The Astrophysical Journal, 924:38 (20pp), 2022 January 1 https://doi.org/10.3847/1538-4357/ac31a8

Core-collapse Supernova Simulations and the Formation of Neutron Stars, Hybrid Stars, and Black Holes

Takami Kuroda[1], Tobias Fischer[2], Tomoya Takiwaki[3], and Kei Kotake[4]
[1] Max-Planck-Institut für Gravitationsphysik, Am Mühlenberg 1, D-14476 Potsdam-Golm, Germany; takami.kuroda@aei.mpg.de
[2] Institute of Theoretical Physics, University of Wroclaw, Plac Maksa Borna 9, 50-204 Wroclaw, Poland
[3] Division of Science, National Astronomical Observatory of Japan, 2-21-1, Osawa, Mitaka, Tokyo 181-8588, Japan
[4] Department of Applied Physics and Research Institute of Stellar Explosive Phenomena, Fukuoka University, Jonan-ku, Fukuoka City, Fukuoka 814-0180, Japan
Received 2021 September 3; revised 2021 October 15; accepted 2021 October 19; published 2022 January 10

Abstract

We investigate observable signatures of a first-order quantum chromodynamics (QCD) phase transition in the context of core-collapse supernovae. To this end, we conduct axially symmetric numerical relativity simulations with multi-energy neutrino transport, using a hadron–quark hybrid equation of state (EOS). We consider four nonrotating progenitor models, whose masses range from 9.6 to 70 $M_\odot$. We find that the two less-massive progenitor stars (9.6 and 11.2 $M_\odot$) show a successful explosion, which is driven by the neutrino heating. They do not undergo the QCD phase transition and leave behind a neutron star. As for the more massive progenitor stars (50 and 70 $M_\odot$), the proto-neutron star (PNS) core enters the phase transition region and experiences the second collapse. Because of a sudden stiffening of the EOS entering to the pure quark matter regime, a strong shock wave is formed and blows off the PNS envelope in the 50 $M_\odot$ model. Consequently the remnant becomes a quark core surrounded by hadronic matter, leading to the formation of the hybrid star. However, for the 70 $M_\odot$ model, the shock wave cannot overcome the continuous mass accretion and it readily becomes a black hole. We find that the neutrino and gravitational wave (GW) signals from supernova explosions driven by the hadron–quark phase transition are detectable for the present generation of neutrino and GW detectors. Furthermore, the analysis of the GW detector response reveals unique kHz signatures, which will allow us to distinguish this class of supernova explosions from failed and neutrino-driven explosions.

Unified Astronomy Thesaurus concepts: Supernova dynamics (1664); Compact objects (288); High energy astrophysics (739); Supernova neutrinos (1666); Gravitational waves (678); Hydrodynamics (1963)

1. Introduction

The final fate of massive stars is the moment of birth of diverse compact stars. Massive stars heavier than $\sim 8\,M_\odot$ undergo gravitational collapse of their iron core once their core mass reaches the Chandrasekhar limit. Thereafter, part or all of the star collapses and becomes a compact remnant star: a neutron star (NS), a black hole (BH), or an *exotic* star. The remnant type is determined mostly by the progenitor mass (Heger et al. 2003). Generally speaking, more massive stars tend to leave behind BHs, and conversely, less massive stars have a greater chance of leaving NSs (Fryer et al. 1999).

The gravitational collapse releases huge amount of gravitational binding energy, part of which is deposited into the stellar envelope. Depending on the progenitor star, the energy deposition can trigger a stellar explosion called a core-collapse supernova (CCSN). The explosion dynamics regulate how much mass is blown off, or equivalently how much mass accretes on the remnant star. Therefore, the detailed explosion dynamics, including the success or failure of the explosion, are the keys to understand the diversity of remnant compact stars.

Two major explosion mechanisms are currently proposed. The first one relies on the complex interplay between neutrinos and the stellar mantle, called neutrino-driven explosion (NDE). It is considered to account for the vast majority of observed CCSNe, showing an explosion energy of $\sim 10^{51}$ erg (for recent reviews, see Janka et al. 2016; Radice et al. 2018; Müller 2020). The other is called magnetorotational explosion (MRE), which takes place if the progenitor star rotates sufficiently fast and is also magnetized (for recent three-dimensional studies, see Mösta et al. 2018; Bugli et al. 2021; Kuroda 2021; Obergaulinger & Aloy 2021). Due to its efficient energy conversion mechanism, the MRE mechanism may explain some exceptional explosive events called hypernovae (Iwamoto et al. 1998; Nomoto et al. 2006), which exhibit one order of magnitude larger explosion energy than the canonical events. Roughly speaking, the NDE and MRE are currently presumed to explain CCSNe of less and more massive stars, respectively.

Recently, another explosion mechanism has gained more attention in the context of both the explosion dynamics and formation process of neutron stars composed of exotic matter at their interiors (see Fischer et al. 2018; Zha et al. 2020). When the energy density becomes sufficiently high, then nuclear—in general, hadronic—matter undergoes a phase transition to the deconfined quark–gluon plasma. Therefore, the solution of quantum chromodynamics (QCD)—the theory for strong interactions with quarks and gluons as the degrees of freedom—predicts a smooth crossover transition at a pseudo-critical temperature in the range of 150–160 MeV (Bazavov et al. 2014; Borsányi et al. 2014; Bazavov et al. 2019). However, this is the case only at vanishing baryon density, and hence cannot be applied to astrophysical applications of compact stellar objects such as neutron stars and supernovae. At high density, phenomenological quark matter models have long been employed in astrophysical studies, based on the common two-phase approach with separate hadronic and quark

matter phases. Such phase transition construction results not only in the transition to the third family of compact stars, known as *hybrid* stars, as an extension to the neutron stars second family, but also in the as-yet incompletely understood question of the nature of the QCD phase transition at high baryon density (see Annala et al. 2020, and references therein). It is likely that low- and intermediate-mass NSs, having masses of $\sim 1.4\,M_{\odot}$, can be explained solely by hadronic equations of state (EOS). More massive NSs with $\sim 2\,M_{\odot}$, the presence of which has been observationally confirmed at high accuracy (see. Demorest et al. 2010; Antoniadis et al. 2013; Cromartie et al. 2020), feature the highest baryon densities encountered in the universe. It is a valid question to ask if a QCD transition occurs at the densities encountered at the interior of such massive pulsars (see Kurkela et al. 2014, and references therein). Furthermore, if confirmed, this is likely to affect our understanding of the core-collapse supernova phenomenology.

This is the origin of the third explosion mechanism, which utilizes the difference in the gravitational binding energy between NSs and hybrid stars. As a consequence, once the central energy density of the PNS enters the phase transition region, the PNS core migrates to a new state, liberating a considerable amount of gravitational potential energy. The latter is directly related to the latent heat, as a consequence of the phase transition construction within the two-phase approach. (for a recent review, see Baym et al. 2018). Assuming a sufficiently strong first-order transition, previous CCSN simulations showed a possible explosion scenario (Sagert et al. 2009; Nakazato et al. 2013; Fischer et al. 2018; Zha et al. 2020), which relies on the energy liberation at the moment of the phase transition. Under such conditions, the PNS core favors a dynamical collapse, rather than a smooth transition, into the hybrid star branch. When the infalling matter collides with a solid surface of the quark core, the dynamical collapse can be halted, depending on the PNS mass. Then it leads to a formation of a strong shock wave, which may blow off the outer envelope. This is the mechanism of the explosion driven by the QCD phase transition (hereafter, phase-transition-driven explosion, abbreviated PDE).

It is intriguing to explore the dependence of the progenitor mass on the PDE dynamics and also on the final remnant property. One can naively expect that progenitors on the less massive side (say $\lesssim 20\,M_{\odot}$) may explode as CCSNe (e.g., Müller et al. 2013; Takiwaki et al. 2016; Vartanyan et al. 2019), probably via the standard NDE mechanism, and leave NSs. This is because, for such low-mass stars, the PDE may not be relevant, as the PNS interior is unlikely to become sufficiently dense to reach the QCD phase transition before the NDE. On the other hand, the more massive stars ($\gtrsim 70\,M_{\odot}$) tend to become failed CCSNe and leave BHs (Kuroda et al. 2018; Shibagaki et al. 2021). Although the progenitor mass threshold, above which they are expected to end up with BH formations, is yet to be understood, some intermediate-mass stars, e.g., $\sim$40–50 $M_{\odot}$ at their zero-age main sequence (ZAMS), are reported to form BHs in the standard neutrino heating mechanism (irrespective of the spatial dimension; see Liebendörfer et al. 2004; Sumiyoshi et al. 2007; Chan et al. 2018; Pan et al. 2018). However, with the aid of the QCD phase transition, these intermediate-mass stars could turn into successful CCSNe, with the remnant being hybrid stars (Fischer et al. 2018). Progenitor mass dependence of phase transition has been studied by Fischer et al. (2020) and Zha et al. (2021), though only in spherically symmetric models.

It is noteworthy that, contrary to the NDE case, the PDE mechanism works even in the spherically symmetric model. There is a consensus that the successful CCSN explosion driven by neutrino heating cannot be achieved under spherical symmetry (1D) (Liebendörfer et al. 2001; Sumiyoshi et al. 2005), except for a few less-massive star models (with $\lesssim 10\,M_{\odot}$, Kitaura et al. 2006). This is because of the inefficient neutrino heating in the absence of lateral hydrodynamic motions in 1D. The mechanism of PDE, on the contrary, does not rely on the neutrino heating, but mostly on the strength of the hydrodynamic bounce of the quark core, i.e., on the QCD phase transition. Therefore, most previous PDE studies have been reported using 1D models (Sagert et al. 2009; Nakazato et al. 2013; Fischer et al. 2018, 2020), and the only multidimensional (multi-D) model reported so far is that of Zha et al. (2020). However, their study focuses mainly on the impacts of phase transition on the gravitational wave (GW) emission using a particular progenitor star with $12\,M_{\odot}$, and the hydrodynamic evolution of the multi-D PDE model is thus currently not well-studied.

There are additional remarkable aspects of the PDE: its relatively large explosion energy of a few times 10^{51} erg (Fischer et al. 2018), and a possible mass window of its progenitor stars. For the latter, intermediate-mass stars with $\sim$40–50 $M_{\odot}$ at ZAMS stage could be potential candidate PDEs, as less massive stars ($\lesssim 20\,M_{\odot}$) may explode solely via the neutrino heating mechanism, while more massive stars can directly collapse into a BH (Heger et al. 2003). According to the stellar evolution models, such intermediate-mass stars experience severe mass loss during their evolutionary stages (e.g., Umeda & Nomoto 2008) and would produce a dense circumstellar medium (CSM). From these facts, the PDE might be able to account for a subclass of CCSNe: the CSM-interacting superluminous SN (hereafter SLSN). This is because the observed light curves of SLSNe, such as SN 2006gy (Smith et al. 2007; Moriya et al. 2013) or SN 2008fz (Drake et al. 2010), can be modeled well by slightly larger explosion energy than normal type IIp SNe (Hamuy 2003), a few times 10^{51} erg, and a dense CSM, with which the SN explosion interacts. We should, however, note that the origins of such superluminous transient events are still under debate. While the abovementioned interaction between type IIn SN ejecta and a dense CSM is indeed one plausible mechanism, other possible scenarios have also been proposed to explain the light curves of SLSNe, such as by pulsational pair instability supernovae (Woosley et al. 2007) or type Ia SNe in CSM (Jerkstrand et al. 2020).

In this study, we perform 2D axially symmetric numerical simulations of the core collapse of massive stars, and we explore the possible impacts of the phase transition on the PNS evolution and the remnant property. We particularly focus on the PDE dynamics in a multi-D model. To this end, we select four massive progenitor stars ranging from $9.6\,M_{\odot}$ to $70\,M_{\odot}$ and use one particular EOS, which considers the first-order phase transition from hadronic matter to quark–gluon plasma (for details, see Fischer et al. 2018; Bastian 2021). The employed supernova model is based on numerical relativity and solves the general relativistic neutrino radiation hydrodynamics equations together with the two-moment (M1) neutrino transport equations (details can be found in Kuroda et al. (2016b)).

We use up-to-date neutrino opacities following Kotake et al. (2018). Our results clearly show a diversity of post-bounce evolution for various progenitor masses. We also discuss their multi-messenger signals: gravitational waves (GWs) and neutrino signals.

This paper is organized as follows. Section 2 starts with a concise summary of our GR radiation-hydrodynamic (RHD) scheme and also describes the initial setup of the simulation. The main results and detailed analysis of the effects of phase transition are presented in Section 3. In Section 4, we discuss multi-messenger signals obtained from computed models. We summarize our results and conclude in Section 5. Note that cgs units are used throughout the paper. Greek indices run from 0 to 3 and Latin indices from 1 to 3, except for ν and ε, which denote neutrino species and energy, respectively.

2. Method and Initial Models

In our full GR RHD simulations, we solve the evolution equations of geometrical variables and the relativistic hydrodynamics together with the energy-dependent neutrino radiation transport. The basic method of solving the evolution equations is the same as for our previous full 3D studies in the Cartesian coordinates (Kuroda et al. 2016b, 2020). The only difference is that we employ the so-called Cartoon method (Shibata 2000; Alcubierre et al. 2001), which allows us to evolve the axisymmetric geometrical variables in the 3D Cartesian coordinates. On the other hand, we use the cylindrical coordinates for the RHD part, which is more suitable for satisfying the conservation laws and solving the conservation equations. The physical domain is on the $y = 0$ plane, and the cell centers of the Cartoon meshes and cylindrical meshes overlap each other. In addition, all geometrical, hydrodynamical, and radiation variables are defined at cell centers.

We follow the collapse and post-bounce evolution of nonrotating progenitor stars with 9.6 $M_\odot$, 11.2 $M_\odot$, 50 $M_\odot$, and 70 $M_\odot$. The progenitor with 9.6 $M_\odot$ (hereafter $z9.6$) is a star with zero metallicity and is considered to be in the lowest mass range of progenitor stars of CCSNe. Its structural feature is a steep density gradient above the iron core that enables a successful explosion even in 1D models (Radice et al. 2017). Another low-mass progenitor model with 11.2 $M_\odot$ ($s11.2$) is a widely used progenitor model with solar metallicity, taken from Woosley et al. (2002). The progenitor model with 50 $M_\odot$ ($s50$) of Umeda & Nomoto (2008) is a blue supergiant star with solar metallicity, and it was used in the previous study of Fischer et al. (2018) to explore a possible scenario of a superluminous SN triggered by the QCD phase transition. The heaviest progenitor star among our set of progenitors is 70 $M_\odot$ ($z70$), with zero metallicity (Takahashi et al. 2014). This progenitor star may form a BH, as was explored by Kuroda et al. (2018) and Shibagaki et al. (2021), and is a suitable model to investigate if the QCD phase transition can turn the failed SN model into a successful one.

In the present study, we implement the EOS of Fischer et al. (2018). It features a phase transition from the DD2 nuclear relativistic mean field model of Typel et al. (2010), with density-dependent meson–nucleon couplings, to the string-flip quark matter EOS. The latter is based on a novel relativistic density functional (RDF) approach, which is build on a mechanism for (de)confinement through a string-like potential that is divergent at vanishing density. Furthermore, linear and higher-order repulsive vector interactions are included in the quark matter phase, following Benić et al. (2015); these interactions give rise to additional pressure contributions at high density. The RDF model, which was developed originally for cold neutron star studies by Kaltenborn et al. (2017), was extended by Fischer et al. (2018) and Bastian (2021) to finite temperatures and arbitrary isospin asymmetry, in order to be applicable to astrophysical studies of core-collapse supernovae in Fischer et al. (2018) and Fischer et al. (2020) as well as binary neutron star mergers in Bauswein et al. (2019). Finite temperature and isospin asymmetry aspects are particularly important, since the conditions for the onset of the phase transition have a strong temperature and charge fraction dependence (see Figure 1 and the phase diagram in Figure 7 of Fischer 2021). Here, we employ the string-flip parameterization denoted as DD2F–RDF 1.2 (see Table 1 in Bastian (2021)). It features densities for the onset of the phase transition of $3.25 \times \rho_{\rm sat}$[5] at zero temperature ($T = 0$) and $1.15 \times \rho_{\rm sat}$ at $T \simeq 50$ MeV (see Table 1 and Figure 1 in Fischer (2021)). The maximum mass of DD2F–RDF 1.2 for cold and nonrotating hybrid stars of 2.16 $M_\odot$ is in agreement with the most precisely known massive pulsar of 2.08 ± 0.07 $M_\odot$ for the PSR J0740 +6620 pulsar obtained by the analysis of Antoniadis et al. (2013), which has been recently revisited by Fonseca et al. (2021). In addition, this hybrid EOS is compatible with the recent neutron star radii constraints. These have been obtained by the NICER collaboration analysis for intermediate-mass neutron stars of the pulsar PSR J0030+0451 in Miller et al. (2019), with a mass of 1.44 $M_\odot$ and a radius of $13.02^{+1.24}_{-1.06}$ km (see also Bilous et al. 2019), as well as for the pulsar PSR J0740+6620, which is a neutron star of about 2 $M_\odot$, by Riley et al. (2021) and Miller et al. (2021), where a radius constraint was deduced of 11.4–16.3 km at the 68% confidence level. We note further that the DD2F nuclear relativistic mean field EOS has been modified from its original DD2 version in order to be consistent with the supersaturation density constraint deduced from the heavy-ion collision data analysis

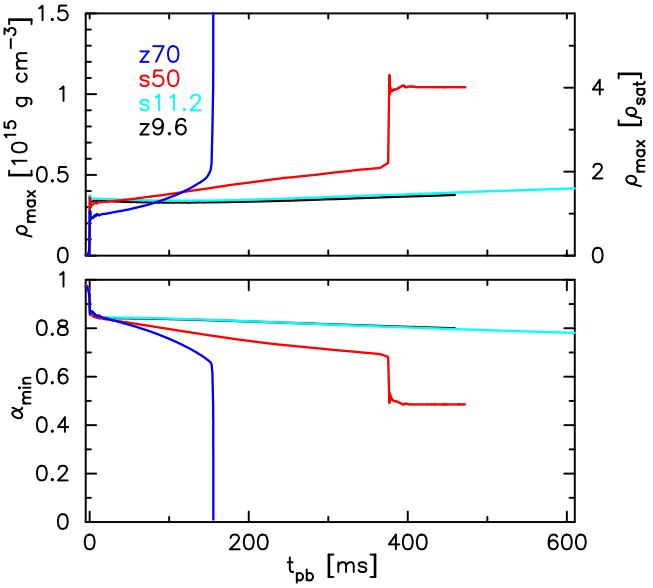

Figure 1. Top panel: evolution of the maximum rest-mass density for all models in units of 10^{15} g cm^{-3} (left axis) and of $\rho_{\rm sat}$ (right axis). Bottom panel: evolution of the central lapse function.

[5] The saturation density has a value of $\rho_{\rm sat} = 2.5 \times 10^{14}$ g cm^{-3} or equivalent in nuclear units 0.15 fm^{-3}.

of the elliptic flow by Danielewicz et al. (2002). For the phase transition construction from DD2F to RDF, a Maxwell-like construction is applied (further details can be found in Bastian 2021).

The 2D axially symmetric computational domain extends to 1.5×10^4 km, for $z70$ and $s50$, and to 7.5×10^3 km, for $s11.2$ and $z9.6$, from the center. The reason for the smaller computational domain for $s11.2$ and $z9.6$ is simply that our EOS tabulation does not cover the required low-density region. In the computational domain, nested boxes with 11(10) refinement levels are embedded for $z70$ and $s50$ ($s11.2$ and $z9.6$), and each nested box contains 64×64 cells so that the finest resolution at the center becomes $\sim$115 m (a detailed resolution study can be found in Appendix A). The neutrino energy space ε logarithmically covers from 1 to 300 MeV with 20 energy bins.

In this study, we use the up-to-date neutrino rates of Kotake et al. (2018). The electron capture rate on heavy nuclei is the most elaborate one, following Juodagalvis et al. (2010). Furthermore, we also take into account the following corrections: the inelastic contributions and weak magnetism corrections of Horowitz (2002) for the charged-current neutrino emission and absorption processes involving the unbound nucleons as well as for the neutral-current neutrino nucleon scattering processes; a correction for the effective nucleon mass (Reddy et al. 1999); the quenching of the axial-vector coupling constant (Carter & Prakash 2002; Fischer 2016); the many-body and virial corrections of Horowitz et al. (2017) for the neutral-current neutrino nucleon scattering rates; effective strangeness contributions reducing the axial-vector coupling constant following Horowitz (2002), also here for both charged-current neutrino emission and absorption processes involving the unbound nucleons as well as for the neutral-current neutrino nucleon scattering processes. Following Melson et al. (2015a), we use $g_A^s = -0.1$ (Hobbs et al. 2016) for the effective strangeness contributions in this work, where this value increases(decreases) the cross section for νp (νn)-scattering.

In the quark matter phase, the description of weak interaction rates based on microscopic calculations is an active field of research (see Berdermann et al. 2016, and references therein), e.g., exploring the role of pairing, which might modify the neutrino opacity significantly in comparison to the simplistic and well-known noninteracting Fermi gas picture. However, such computations are very demanding and hence not feasible in simulations of astrophysical applications. Instead, we employ the standard weak rates in quark matter featuring baryons. These include the charged-current absorption reactions and the inelastic neutrino–nucleon scattering processes. Therefore, we reconstruct the baryon and charge chemical potentials, $\mu_{\rm B}$ and μ_Q, from the up- and down-quark chemical potentials, μ_u and μ_d, as follows:

$$\mu_{\rm B} = 2\mu_d + \mu_u, \quad \mu_Q = \mu_u - \mu_d. \tag{1}$$

These in turn give rise to the neutron and proton chemical potentials, $\mu_n = \mu_{\rm B}$ and $\mu_p = \mu_{\rm B} + \mu_Q$, respectively, as well as the corresponding number densities for neutrons and protons, n_n and n_p, which are being reconstructed from the up- and down-quark number densities, n_u and n_d,

$$n_n = \frac{1}{3}(2n_d + n_u), \quad n_p = \frac{1}{3}(2n_u + n_d)\,. \tag{2}$$

This simplification is justified because, at the conditions where quark matter appears, neutrinos of all flavors are entirely trapped. The diffusion timescale is on the order of seconds and cannot change significantly, even if the opacity for the corresponding weak interactions with quarks should strongly decrease, because neutrinos would still be trapped through a variety of other, purely leptonic weak processes, such as neutrino scattering on electrons and positrons, as well as neutrino pair reactions. Only on a supernova simulation timescale on the order of seconds, when neutrinos would start to diffuse from the quark matter phase, can the aforementioned approximations no longer be applied.

3. Results

In this section, we present the results of our simulations. We begin with a description of the overall dynamics of all the models. After that, we focus on a particular model, $s50$, and explain its second collapse and bounce in detail.

3.1. Collapse of Stellar and PNS Core

Figure 1 shows the evolution of maximum density and minimum lapse function for all models, from which we can gain a first glimpse of the overall dynamics. After the central density exceeds the nuclear saturation density, the stellar core collapse halts and the core experiences the first core bounce due to stiffening of the nuclear EOS. We define the moment of core bounce, $t_{\rm pb} = 0$, when the maximum rest-mass density is reached. It corresponds to the following values for the maximum: central density of $\rho_{\rm max} = 3.81$, 3.92, 3.62, and 2.73×10^{14} g cm^{-3} for models $z9.6$, $s11.2$, $s50$, and $z70$, respectively. Roughly speaking, therefore, the maximum density at bounce has an inverse relation with the progenitor mass. This is related to the temperatures obtained in these simulations, which are highest(lowest) for the more(less) massive progenitors, i.e., the thermal pressure additionally supports the halt of the stellar core collapse and the subsequent core bounce.

After the first bounce, the maximum density again increases with time in all models, due to the continuous mass accretion prior to the possible onset of a shock revival. While the less massive progenitor stars, $z9.6$ and $s11.2$, show only a slight increase compared to the other two more massive stars, the model $z70$ shows the most rapid increase rate, which entails the highest rate of mass accretion. Consequently, $z70$ reaches the highest central temperatures and luminosities during the post-bounce evolution (see the thin white line in Figure 2 and the top panel of Figure 13). At the same time, $z70$ exhibits an accelerated decrease in the minimum lapse function $\alpha_{\rm min}$, as illustrated in the bottom panel of Figure 1, which decreases below $\lesssim$0.01 at $t_{\rm pb} \sim 155$ ms, and we observe the formation of the apparent horizon. At our final simulation time for $z70$, i.e., less than a millisecond after the apparent horizon appears, its circumferential radius is $\sim$2.29 km, with its corresponding mass being $\sim 2.40\,M_\odot$. Since the initial condition is spherically symmetric, the apparent horizon essentially preserves the spherically symmetric property, with its deviation from spherical symmetry being less than 0.1%. We note that the size of the quark core at this moment has a radius of $\sim$1.8 km, which is well within the apparent horizon and is thus causally disconnected from the outside. A comparison with the study of

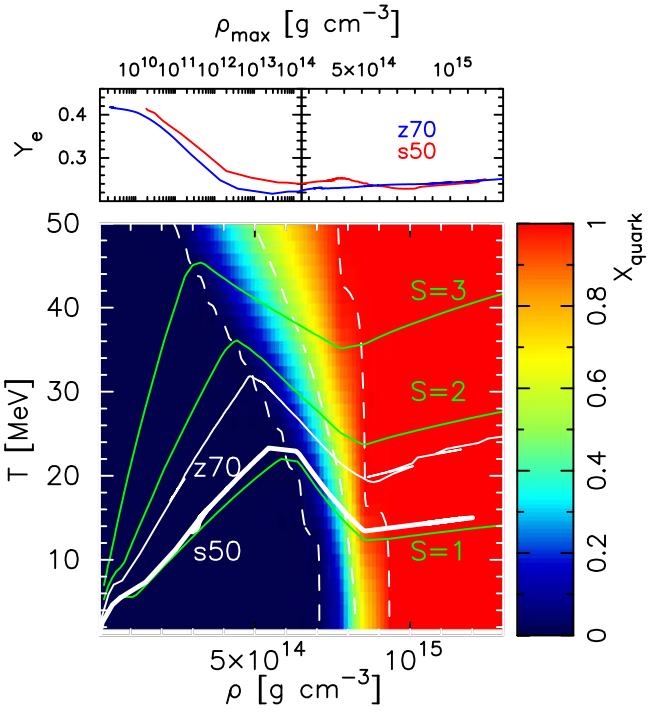

Figure 2. Top panel: evolution of the central Y_e as a function of the central rest-mass density, ρ_{max}, for the models $s50$ (red line) and $z70$ (blue line). Bottom panel: phase diagram of the DD2F–RDF 1.2 hybrid-EOS, showing the quark volume fraction X_{quark} defined in Bastian (2021), in the density–temperature plane with a fixed electron fraction of $Y_e = 0.25$, which is a typical central value after bounce for both $s50$ and $z70$. The white thick(thin) line denotes the evolutionary path of quantities for $s50(z70)$. The green and white dashed lines are showing the curves of constant entropy per particle of $s = 1\ k_B$, $2\ k_B$, and $3\ k_B$, and contours of $X_{quark} = 0.01$ (left), 0.5 (middle), and 0.99 (right), respectively.

Shibagaki et al. (2021), where the same $z70$ progenitor model was used, shows the black hole formation at a significantly later post-bounce time of $t_{pb} \simeq 230$ ms. This is attributed to the different, purely hadronic EOS of Lattimer & Swesty (1991) used in the supernova simulations of Shibagaki et al. (2021), which are based on 3D general relativistic neutrino-radiation hydrodynamics simulation. In their case, the PNS collapse and black hole formation are induced due to the enclosed PNS mass reaching the maximum mass of the hadronic EOS. In contrast here, the PNS collapse is due to reaching the critical conditions for the onset of the phase transition. The phase boundaries, as well as their temperature dependence, are marked as green dashed lines in Figure 2, for the onset of the hadron–quark mixed phase (left) and for the pure quark matter phase (right). It becomes evident that the evolution proceeds through the hadron–quark mixed phase into the pure quark matter phase. However, when the second collapse halts in the pure quark matter phase, and even though a second shock wave has formed in compliance with the previous study of Fischer et al. (2018), the enclosed mass of about $2.7\,M_\odot$ (see Figure 3) exceeds the maximum mass given by the DD2F–RDF 1.2 hybrid EOS and a black hole forms eventually.

The $s50$ model takes an intermediate evolutionary path between the less massive ($z9.6$ and $s11.2$) and the most massive ($z70$) progenitor stars. The maximum density increases significantly faster here than in the lower-mass models, due to a higher post-bounce mass accretion rate, though slower than for $z70$. At $t_{pb} \sim 376$ ms, when the maximum density reaches slightly above two times the saturation density, the PNS core enters the phase transition region, as illustrated via the thick white line in Figure 2. Similarly as for the $z70$ simulation, for $s50$ the central PNS becomes gravitationally unstable and collapses once a sufficiently large amount of the PNS interior enters the hadron–quark mixed phase, where the EOS softens substantially in comparison to the pure hadronic and quark matter phases at lower and higher density, respectively. During this second collapse, the maximum density increases rapidly from $\rho_{max} \simeq 2 \times \rho_{sat}$ to slightly above $\rho_{max} \gtrsim 4 \times \rho_{sat}$ (see Figure 1). At such a high density, baryons are completely dissociated into quarks, and the stiffness of EOS again increases, mediated by the repulsive vector interactions. Consequently, the NS collapse halts, and the second core bounce occurs at $t_{pb} = 376.6$ ms. The second bounce time seen in the model $s50$ is considerably earlier than the finding of about 1.2 s in Fischer et al. (2018). We attribute the reason for this to the different hybrid EOS applied in Fischer et al. (2018), corresponding to the DD2–RDF 1.1 nomenclature of Bastian (2021). It features a generally higher onset density for the hadron–quark phase transition, on the order of $3.5 \times \rho_{sat}$ at $T = 0$, as well as a different temperature dependence. Further differences in the simulations may arise due to the different hydrodynamics scheme of the supernova model of Fischer et al. (2018), which is based on an adaptive Lagrangian mass grid and differs from the one in this study. Furthermore, we have checked if the spatial resolution can influence on the evolution up to and including second bounce, and found a rough numerical convergence, which is discussed in Appendix A.

Figure 2 depicts how the central PNS evolves in the phase diagram of the DD2F–REF 1.2 hybrid EOS. The top panel shows the evolution of the central Y_e as a function of the central rest-mass density for the models $s50$ (red line) and $z70$(blue), with $Y_e \simeq 0.25$ for both simulations. The bottom panel exhibits the phase diagram of the hybrid EOS employed, with the color-coding indicating the quark volume fraction, X_{quark}, in the density–temperature plane for a fixed $Y_e = 0.25$. The white thick and thin solid lines denote evolutionary paths of the central density and temperature for $s50$ and $z70$, respectively. The green lines show curves of constant entropy per particle of $s = 1\ k_B$, $2\ k_B$, and $3\ k_B$, and the vertical white dashed lines correspond to $X_{quark} = 0.01$, 0.5, and 0.99.

In both models $s50$ and $z70$, the central region evolves along a nearly constant entropy path after the first bounce due to the adiabatic compression. This lasts until it reaches the purely quark matter phase, i.e., where $X_{quark} = 1$. From the phase diagram, we clearly see a temperature dependence of the initiation of the hadron quark mixed phase, i.e., the left vertical white dashed curve. It shows that the mixed phase appears at lower density for matter with higher temperature or entropy. It turns out that the model $z70$, possessing higher core entropy, enters the phase transition region at a slightly lower density of $\rho_{max} \simeq 5 \times 10^{14}$ g cm^{-3}, compared to the value of $\rho_{max} \simeq 6 \times 10^{14}$ g cm^{-3} in $s50$. After the central region enters the pure quark matter phase, we witness multiple core bounces for $z70$, due to the stiffening of EOS that produces a standing shock front. However, the mass accretion rate is extremely high, on the order of $\sim 4\,M_\odot$ s^{-1}, measured on the shock surface at the second collapse, and the shock front cannot propagate outward to blow off the outer envelope. Instead, ρ_{max} increases continuously and a black hole is quickly formed as already explained. On the other hand, the maximum density for $s50$ does not continuously increase once its PNS interior

Table 1
List of Models and their Simulation Results, Showing the Compactness Parameters, ξ_M, Measured at Two Different Mass Coordinates of 1.5 $M_\odot$ and 2.5 $M_\odot$, the Remnant Masses, $M_{\rm remnant}$, the Mass of the Quark-matter Core, $M_{\rm quark}$, the Explosion Time, $t_{\rm exp}$, and the Final Simulation Time, $t_{\rm final}$

Model	$\xi^{\rm b(i)}_{1.5}$	$\xi^{\rm b(i)}_{2.5}$	$M_{\rm remnant}$ ($M_\odot$)	$M_{\rm quark}$ ($M_\odot$)	$t_{\rm exp}$ (ms)	$t_{\rm final}$ (ms)
*z*9.6	(2.2×10^{-4})	(7.6×10^{-5})	1.37	⋯	167	459
*s*11.2	$2.4(1.8) \times 10^{-1}$	(5.0×10^{-3})	1.40	⋯	503	650
*s*50	2.3(1.6)	$1.9(1.9) \times 10^{-1}$	1.83	1.35	384	450
*z*70	4.0(1.1)	1.6(1.0)	2.65	1.88	⋯	155

Notes. We evaluate ξ_M at core bounce and at the initial data, denoted by $\xi^{\rm b}_M$ and $\xi^{\rm i}_M$ (values in parentheses), respectively. Note that our calculation domain does not contain 1.5 $M_\odot$ for *z*9.6 or 2.5 $M_\odot$ for *s*11.2, and we omit the corresponding compactness parameters at bounce ξ^b_M from the table. Explosion time $t_{\rm exp}$ denotes the post-bounce time when the average shock radius reaches $r = 1000$ km.

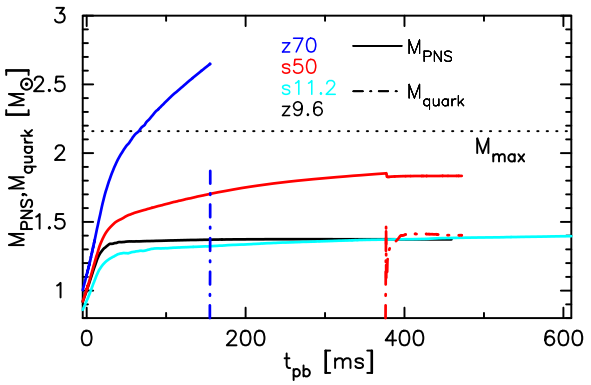

Figure 3. Post-bounce evolution of the rest mass of the PNS mass $M_{\rm PNS}$ (solid lines) and proto-quark star mass $M_{\rm quark}$ (dashed) for all models. The horizontal dotted line marks the maximum mass at $T = 0$ of $M_{\rm max} = 2.16\ M_\odot$ for the current EOS. $M_{\rm quark}$ for *z*9.6 and *s*11.2 is zero because the hadron–quark phase transition region is not reached during our simulation time of $t_{\rm pb} \lesssim 600$ ms.

transforms into a quark matter core. In Figure 1, $\rho_{\rm max}$ shows a single bounce and then quickly settles into a new value of $\rho_{\rm max} \simeq 1.05 \times 10^{15}$ g cm^{-3} after a rapid ring-down phase. At the same time, the minimum lapse $\alpha_{\rm min}$ also decreases from ∼0.7 to ∼0.5 across the second core bounce. The second bounce creates an energetic hydrodynamic shock wave due to the stiffening of EOS. In contrast to *z*70, which has a significantly higher mass accretion rate, the shock front propagates outward with a relativistic velocity of about two-thirds of the speed of light, because of a lower mass accretion rate of about 0.33 $M_\odot$ s^{-1} measured on the shock surface at the second core collapse. The shock evolution will be discussed in Section 3.2.

The qualitative difference between the BH formation model (*z*70) and the explosion model (*s*50) can be explained by the evolution of the PNS mass. In Figure 3, we plot the PNS mass $M_{\rm PNS}$ (solid lines) and proto-quark star mass $M_{\rm quark}$ (dashed) for all models. The latter is defined via the quark volume fraction exceeding one percent. It has been introduced in Fischer et al. (2018), and further details, including the phase transition construction, can be found in Bastian (2021). We define the PNS surface by the region where the rest-mass density drops below 10^{10} g cm^{-3}.

In contrast to the *z*70 model, the baryon mass enclosed inside the PNS for *s*50 of about 1.83 $M_\odot$ is well below the maximum gravitational mass of DD2F–RDF 1.2 after the hadron–quark phase transition (see Figure 3). Note that the maximum allowed mass for hot neutron stars can be increased by ∼0.2–0.4 $M_\odot$, compared to their corresponding cold case, due to the corresponding additional pressure support from hot matter (see Hempel et al. 2012). The nascent PNS for *s*50 features a massive quark matter core of about 1.43 $M_\odot$. The case of *z*70 is similar: a strong second hydrodynamics shockwave forms as a result of the phase transition. However, in the case of *s*50, the remnant PNS is semistable, e.g., with respect to radial and nonradial perturbations, such that a black hole formation is not observed. The dynamics of the second shock wave have important consequences for the supernova explosion dynamics, which will be discussed below.

None of the lighter progenitor models, *z*9.6 and *s*11.2, reach the conditions required for the hadron–quark phase transition in our simulation times of less than ∼600 ms after bounce. Instead, these two models show the explosion driven by neutrino heating. This will be explained in detail in Section 3.2. It is noteworthy that the maximum density continues to increase slightly after the explosion begins. If the central density increases at the same rate at the final simulation time $\dot{\rho}_{\rm max} \sim 10^{14}$ g cm^{-3} s^{-1}, we estimate that it will exceed $2 \times \rho_{\rm sat}$ at $t_{\rm pb} \sim 1.5$ s in both models and the hadron–quark phase transition may occur during the subsequent deleptonization phase of the nascent NS. However, we note here also that the phase transition onset mass of DD2F–RDF 1.2 for cold neutron stars, i.e., the mass threshold for the hybrid star branch, lies above 1.37 $M_\odot$. Hence, in the case that the phase transition were to occur, we expect that only a tiny fraction, if any, of the neutron star's interior would consist of pure quark matter.

In Table 1, we list a summary of progenitor models and their final fates. The compactness parameter ξ_M measures the ratio of mass $M(M_\odot)$ and radius R_M, where the latter term R_M expresses the radius, which encloses the mass M (O'Connor & Ott 2011), and is in units of 1000 km. Regarding the compactness of progenitor star, ξ, *z*70 shows the highest value. O'Connor & Ott (2011) discussed a relation between the bounce compactness $\xi^{\rm b}_{2.5}$ and BH formation time. According to their result, BH formation time is less than a few 100 ms for very massive stars having $\xi^{\rm b}_{2.5} \gtrsim 1.5$, which is in accordance with the current model *z*70. Here, *s*50 forms a hybrid star, with its quark core and total PNS mass reaching 1.43 and 1.83 $M_\odot$, respectively. Both *z*9.6 and *s*11.2, which have a small compactness

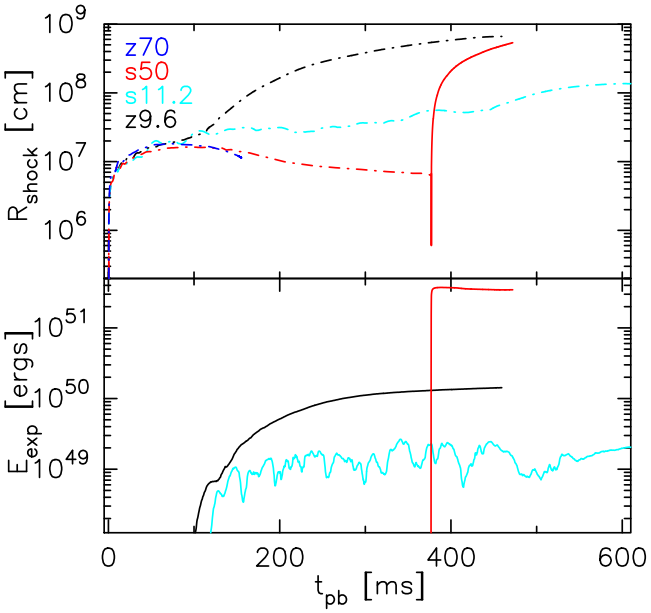

Figure 4. Post-bounce evolution of the averaged shock radii $R_{\rm shock}$ (top panel) and of the diagnostic explosion energy $E_{\rm expl}$ (bottom panel) for all models. In the upper panel, we distinguish the core bounce shock (denoted by the dashed–dotted line) and the second bounce shock (solid).

parameter, show almost the same PNS mass 1.37 $M_\odot$, with their evolution showing a plateau behavior (see black and cyan lines in Figure 3).

3.2. Explosion Dynamics

In this section, we discuss the explosion dynamics for models *z*9.6, *s*11.2, and *s*50. As *z*70 does not explode, its $E_{\rm exp}$ is zero. Figure 4 exhibits the time evolution of averaged shock radii $R_{\rm shock}$ (top panel) and diagnostic explosion energy $E_{\rm exp}$ (bottom). We note that $E_{\rm exp}$ does not take into account the binding energy of the stellar envelope. In addition, nuclear recombination and the associated nuclear burning energy generation are also neglected.

We begin with *z*9.6. From its shock evolution (black curve in Figure 4), we see that the shock expands slowly at initial times up to about 100 ms post-bounce. After about 120 ms post-bounce, this model enters a shock runaway phase. The shock front reaches 1000 km at $t_{\rm pb} = 167$ ms. At the same time, the diagnostic explosion energy $E_{\rm exp}$ starts increasing and eventually reaches a value of 1.4×10^{50} erg, when the shock front reaches the outer boundary of the calculation domain. In Melson et al. (2015b) and Radice et al. (2017), the authors also performed multi-D SN simulations using the same 9.6 $M_\odot$ progenitor star. Although the detailed numerical setups are different in each study, e.g., different hydrodynamics schemes, grids, neutrino transport, and weak rates, the shock and diagnostic explosion energy evolution show quantitative behavior. Melson et al. (2015b) and Radice et al. (2017) report $E_{\rm exp} \sim 8 \times 10^{49}$ erg and $\sim 1.1 \times 10^{50}$ erg, respectively, at $t_{\rm pb} = 400$ ms, where the latter study takes into account the gravitational binding energy of the envelope, which is merely -2×10^{48} erg (see Melson et al. 2015b). Our diagnostic explosion energy is within a range of uncertainty due to different numerical setups, and we thus find results consistent with those of previous studies for model *z*9.6.

For the other low-mass model *s*11.2, the average shock radius steadily increases without any visible shock stagnation, similarly to *z*9.6, but at a somewhat slower rate. This is attributed to the extended silicon–sulfur layer for this progenitor model, which is absent for *z*9.6. It results in higher mass accretion rates post-bounce for *s*11.2, which in turn slow down the neutrino-driven shock expansion. Figure 4 shows that the mean shock radius $R_{\rm shock}$ reaches 1000 km at $t_{\rm pb} \sim 503$ ms and the diagnostic explosion energy reaches $3\text{–}4 \times 10^{49}$ erg at the end of the simulation. These values are in quantitative agreement with those in Müller (2015), in which the author conducted a relativistic 2D CCSN simulation for the same 11.2 $M_\odot$ progenitor model. Although the employed EOS and neutrino opacities are different, and comparison is not straightforward, his corresponding 2D model shows an evolution similar to that of *s*11.2 in this study. The neutrino-driven supernova explosion observed for this low-mass model *s*11.2 is in qualitative agreement with the results reported by other groups based on axially symmetric simulations (see Buras et al. 2006; Marek & Janka 2009; Takiwaki et al. 2014; Nagakura et al. 2018). More controversial are the recent 3D supernova simulations of this progenitor model (e.g., Takiwaki et al. 2012; Tamborra et al. 2014; Takiwaki et al. 2016), which is an active subject of research.

In comparison to these less massive progenitor stars, *s*50 shows a continuous shock recession once the shock stagnates around $t_{\rm pb} \sim 100$ ms. The recession lasts until the second collapse occurs (see Figure 4). The red line in the top panel shows that the averaged shock radius eventually shrinks to $R_{\rm shock} = 62$ km. Then, concomitantly with the second bounce, a strong second shock wave is produced at the surface of quark core, located at around $r \sim 7$ km. This shock front overtakes the preceding standing shock front at $r = 62$ km and propagates further out with a relativistic velocity, i.e., within a few ms after the second bounce, the shock front exceeds $r = 1000$ km. Simultaneously, the diagnostic explosion energy rises continuously, and reaches its asymptotic value of $E_{\rm exp} \sim 3.5 \times 10^{51}$ erg. Afterward, $E_{\rm exp}$ shows nearly a constant value throughout the runaway explosion phase. We estimate that the gravitational binding energy of the envelope is roughly -4.0×10^{50} erg, and thus the asymptotic explosion energy would be around 3×10^{51} erg. In view of the explosion dynamics, similarly as was discussed in Fischer et al. (2018), our model *s*50 supports that these massive progenitor stars could be the progenitors of a kind of superluminous supernova event, (see the discussions in Smith et al. (2007) and Moriya et al. (2013), and references therein), if a sufficiently strong hadron–quark phase transition occurs.

Next, to illustrate the dynamics at the second collapse and in the subsequent explosion phase, we plot spherically averaged profiles of the rest-mass density ρ and quark fraction $X_{\rm quark}$ (top left panel), entropy s (top right panel), electron fraction Y_e (bottom left panel), and the radial component of the three-velocity v^r (bottom right panel) in Figures 5 and 6, at selected time slices.

Figure 5 shows profiles before second bounce $t_{\rm p2b} < 0$, where $t_{\rm p2b}$ denotes the post-second-bounce time and is written in the top right panel. From the density and radial velocity profiles, we see that the second collapse takes place within a fraction of a millisecond. At $t_{\rm p2b} = -0.49$ ms (black lines), the radial velocity profile shows a nearly hydrostatic profile ($v_r \sim 0$) with a slight infalling sign inside the PNS. At the same time, quarks are

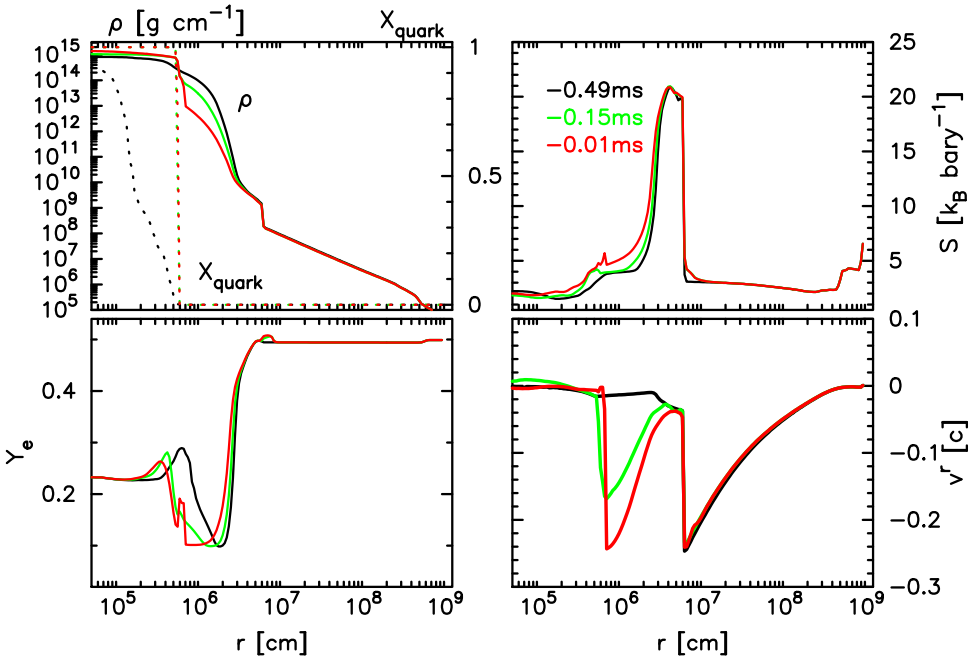

Figure 5. Radial profiles of the rest-mass density ρ (solid lines) and quark fraction $X_{\rm quark}$ (dotted), entropy per particle s, electron fraction Y_e, and radial component of the three-velocity $v^r \equiv u^r/u^t$ for the model $s50$ at different times before the second bounce, denoted as $t_{\rm p2b}$, corresponding to the onset and proceeding collapse of the PNS due to the hadron–quark phase transition.

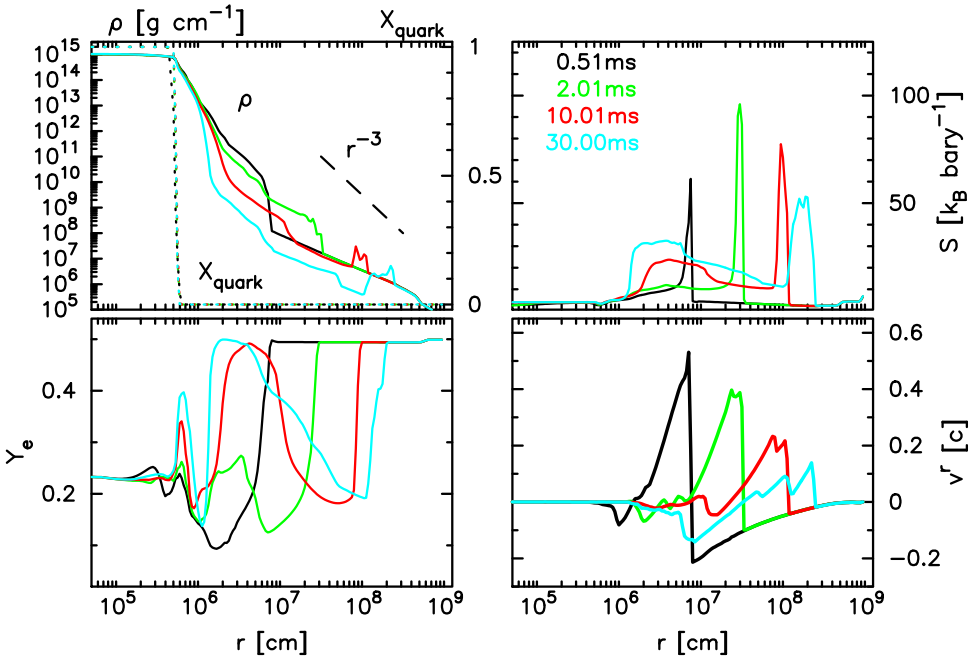

Figure 6. The same as Figure 5, but for different time slices after the second bounce. In the density profile, we show the slope of r^{-3} as a dashed line.

already partially deconfined, showing $X_{\rm quark} \sim 0.9$ at the center. We note that quarks are completely confined in hadronic matter, i.e., $X_{\rm quark} = 0$, up until $\sim$1 ms before the second bounce, which is a major difference from Zha et al. (2020). Shortly after that, the PNS core collapses with a relativistic speed of $\sim 0.25c$ (see the red line in the v^r profile) and the PNS core transforms into a quark core with $X_{\rm quark} = 1$. Meanwhile, the entropy (top right) and Y_e (bottom left) do not show any noticeable changes compared to $X_{\rm quark}$ and v^r.

After the second bounce happens, the hydrodynamic profiles change considerably. The radial velocity profile shows a relativistic outward shock propagation immediately at $t_{\rm p2b} = 0.51$ ms, and already at this moment, the entropy behind the shock reaches $s \geqslant 60\ k_B$ baryon^{-1}. In the subsequent phase, however, its propagation speed decreases gradually as clearly be seen in the bottom right panel. At $t_{\rm p2b} = 30$ ms, the shock decelerates to $\sim 0.1c$ (cyan line in the bottom right panel). The entropy behind the shock also decreases noticeably from $\sim$100 k_B baryon^{-1} at $t_{\rm p2b} = 2$ ms to $\sim$50 k_B baryon^{-1} at $t_{\rm p2b} = 30$ ms. Furthermore, a density bump is formed around $r \sim 10^8$ cm at $t_{\rm p2b} = 10$ ms. All of these facts indicate that the shock front propagates in a dense low-entropy medium and is substantially

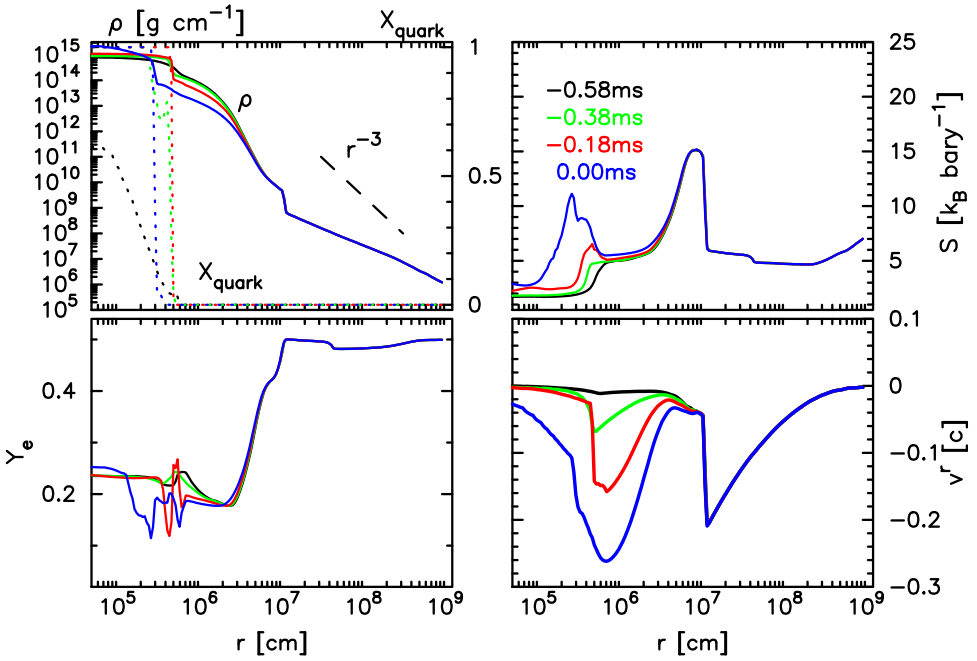

Figure 7. The same as Figure 6, but for model $z70$ at several time slices relative to the final simulation time denoted in the top right panel. The circumferential radius of AH is $r \sim 2.29$ km at the final simulation time.

decelerated. Indeed, from the top left panel in Figure 6, the angle averaged density profile shows a shallower density gradient than the slope of r^{-3} at $10^7\,\mathrm{cm} \lesssim r \lesssim 5 \times 10^8$ cm. In such a dense environment, the shock can be decelerated very efficiently (Sedov 1959; Wongwathanarat et al. 2015), resulting in development of Rayleigh–Taylor (RT) instabilities, which we will describe later.

The Y_e profile also shows a remarkable feature. The low-Y_e materials, which are initially located in the Y_e trough just above the PNS surface $r \sim 20$ km (see black line in the bottom left panel), are ejected along with the explosion, since the explosion is initiated on the quark core surface at $r \sim 7$ km, i.e., underneath the Y_e trough. At $t_{\rm p2b} = 30$ ms, those low-Y_e ejecta are reaching $r \sim 10^8$ cm and produce a steep Y_e composition gradient across the shock surface. We also find a high-Y_e and high-entropy region, for instance, with $s \sim 30\ k_B$ baryon^{-1} and $Y_e \sim 0.5$ around $r \sim 5 \times 10^6$ cm at $t_{\rm p2b} \geqslant 30$ ms. These components are produced due to a powerful neutrino irradiation.

It is informative to show the second "bounce" in model $z70$, as it is associated with the BH formation. Figure 7 is the same as Figure 6, but for model $z70$. Time is measured relative to the final simulation time, i.e., t–$t_{\rm final}$, and denoted in the top right panel. At t–$t_{\rm final} = -0.58$ ms, the highest value for $X_{\rm quark}$ is $\sim$0.6 and thus the quark core is still not formed. The inner core is showing the initiation of second collapse, as can be seen from the black line in the bottom right panel, which marginally shows negative radial velocities at $r \lesssim 5$ km. Afterward, the second collapse accelerates and the quark core is immediately formed. At t–$t_{\rm final} = -0.38$ and -0.18 ms (green and red lines), the shock surface is formed at $r \sim 5$ km, as is the quark core surface. In contrast to the less massive progenitor model $s50$, the second collapse cannot be halted even after the quark core formation, which supplies an additional pressure support. Both the shock and quark core surfaces continuously shrink with no mass ejection (blue line in the velocity profile). At the final simulation time, the shock front recedes to $r \sim 2.3$ km, where the AH appears. At this moment, the quark core surface is located at $r \sim 3$ km, which is above the AH (see the blue dotted line in the top left panel).

A combination of the aforementioned shock deceleration and steep gradient of Y_e results in a very remarkable multi-D hydrodynamic feature. To illustrate it, we depict 2D profiles of the shocked region at several time slices in Figure 8. We select four time slices: $t_{\rm pb} \simeq 150$ ms, as a representative of normal post-bounce structure in Figure 8(a); $t_{\rm pb(p2b)} = 390(14)$ in Figure 8(b); 416(40) in Figure 8(c); and 461(85)ms in Figure 8(d), as an example after the second bounce. Each panel consists of four panels, in which we plot: logarithmic density $\log_{10}(\rho\ [\mathrm{g\,cm^{-3}}])$ (in top left mini-panel), entropy per particle s [$k_{\rm B}$] (top right), temperature T [MeV] (bottom left), and electron fraction Y_e (bottom right) for model $s50$.

Top left panel shows normal convective motions driven mainly by neutrino heating. At $t_{\rm pb} = 150$ ms, the shock front is located at $r \sim 140$ km and high-entropy ($s \sim 15\ k_{\rm B}$ baryon^{-1}) convective bubbles are seen behind it. In the post-second-bounce phase, the shock expands initially with a relativistic speed, though it starts decelerating already at $t_{\rm p2b} \gtrsim 10$ ms. Indeed, from the density contour at $t_{\rm pb(p2b)} = 390(14)$ ms (top right panel), we see a dense shell located between $10^8\,\mathrm{cm} \lesssim r \lesssim 1.5 \times 10^8$ cm. Within the shell, its rest-mass density exceeds $\rho = 10^7\ \mathrm{g\,cm^{-3}}$, which is approximately one order of magnitude larger than the value of its surroundings. A particularly interesting feature is seen on the inner edge of the shell at $r \sim 10^8$ cm, where the density has a negative radial gradient. The deceleration of the dense shell produces an effective outward acceleration in the comoving frame, acting on the shell component. Therefore, it fulfills the condition for development of the Rayleigh–Taylor instability. As a consequence, higher-density materials, which are initially located more inward, penetrate into the lower-density side and the well-known mushroom-like structures are formed. Those mushroom-like plumes are composed of neutron-rich material with $Y_e \lesssim 0.3$ (see bottom right mini-panel at $t_{\rm pb(p2b)} = 390(14)$ ms).

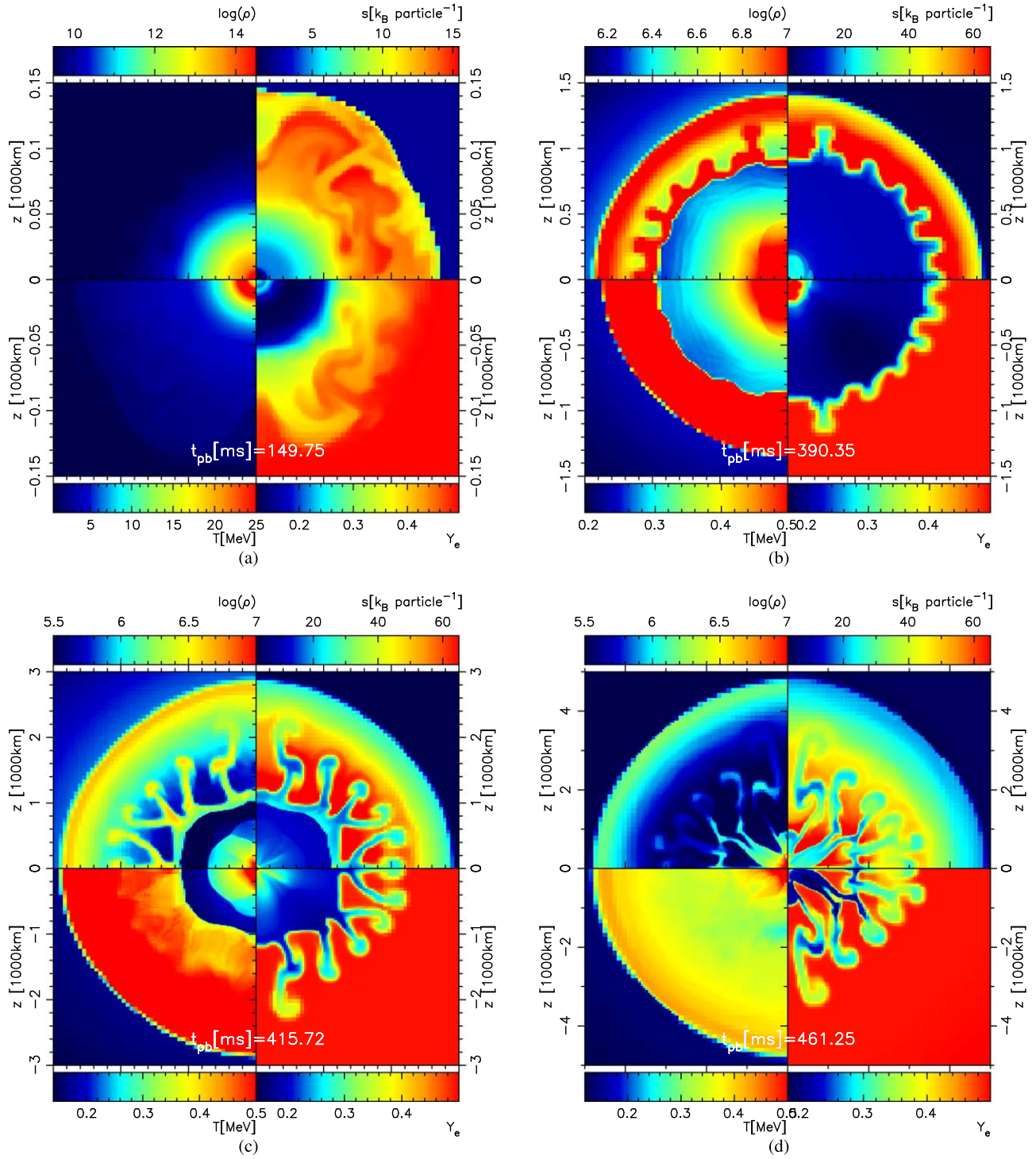

Figure 8. Snapshots of the $x-z$ plane for the logarithmic density $\log_{10}(\rho\ [\mathrm{g\ cm^{-3}}])$ (top left panels), entropy per particle s [k_B] (top right panels), temperature T [MeV] (bottom left panels), and Y_e (bottom right panel) for $s50$, at different time slices $t_\mathrm{pb} = 150$ ms in graph (a) as a representative of the normal structure during the post-bounce phase prior to the hadron–quark phase transition, as well as at $t_\mathrm{pb}(t_\mathrm{p2b}) = 390(14)$ in graph (b), 416(40) in graph (c), and 461(85)ms in graph (d) after the second bounce.

From Figures 8(c) and 8(d), one can find how effectively those plumes, associated with the Rayleigh–Taylor instability, transport the low-Y_e material outward. The low-Y_e plumes are growing at $r \gtrsim 10^8$ cm. At such a distant region from the central hot PNS, neutrino irradiation is significantly weak and neutrino absorption basically does not occur. Consequently, the Y_e of the ejecta basically does not change except through the hydrodynamic mixing process. The radial three-velocity of the plumes is roughly $v^r \sim 0.1c$ at our final simulation time of $t_\mathrm{pb(p2b)} = 475(100)$ ms, and approaches nearly a steady-state value. Fischer et al. (2020) reported an r-process nucleosynthesis calculation based on spherically symmetric explosion models triggered by the PDE mechanism. According to their results, the explosion can indeed transport low-Y_e material to the distant region $r \gtrsim 10^{8-9}$ cm, though the Y_e value tends to become higher ($\gtrsim 0.35$) compared to this study. This is simply

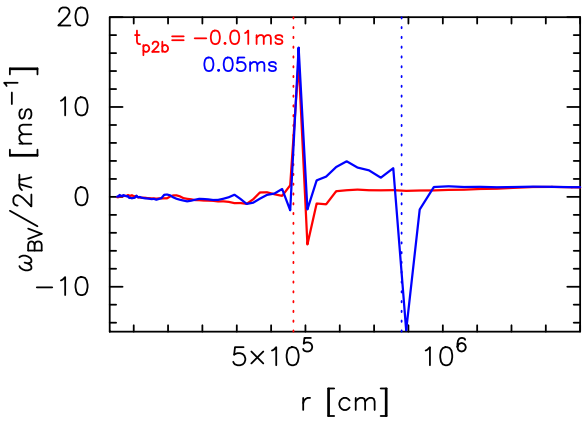

Figure 9. Spherically averaged spatial profiles of the Brunt–Väisälä frequency ω_{BV} for *s*50 around the second bounce. Here, we focus only on the region above the quark-matter core, and we select two representative time slices at $t_{p2b} = -0.01$ ms (red line) and $t_{p2b} = 0.05$ ms (blue line). The vertical dashed lines indicate the averaged radii of the second bounce shock. Negative ω_{BV} indicates a convectively unstable region based on the Ledoux criterion.

due to the absence of the RT mixing under the spherically symmetry. Therefore, with the aid of the RT mixing, the low-Y_e components can be more efficiently ejected and may significantly influence the nucleosynthetic yields, which will be reported elsewhere.

The Rayleigh–Taylor instability can be seeded not only by the inhomogeneous structure behind the standing shock surface (see the top left panel at $t_{pb} \sim 150$ ms in Figure 8), but also by the convective motions inside the quark core itself. To explain this, we evaluate the Brunt–Väisälä frequency ω_{BV} and plot its spherically averaged spatial profile around the second bounce in Figure 9. Here, we follow the same procedure as described in Müller et al. (2013) to evaluate ω_{BV} (see their Equation (14)) in relativistic form as follows:

$$\omega_{BV}{}^2 = \frac{\alpha}{\rho h \phi^4}\frac{\partial \alpha}{\partial r}\left(\frac{\partial \rho(1+\epsilon)}{\partial r} - \frac{1}{c_s^2}\frac{\partial P}{\partial r}\right). \quad (3)$$

Using these expressions, the regions with positive and negative $\omega_{BV}{}^2$ correspond to the convectively stable and unstable regions, respectively. In Figure 9, we plot $\omega_{BV}/2\pi$ while slightly modifying the expression of Equation (3) to be $\omega_{BV} = \mathrm{sgn}(\omega_{BV}{}^2)\sqrt{|\omega_{BV}{}^2|}$, so that the new ω_{BV} becomes a real number with its positive and negative values indicating the convectively stable and unstable regions, respectively. In the figure, we select two time slices across the second bounce, represented by red ($t_{p2b} = -0.01$ ms) and blue ($t_{p2b} = 0.05$ ms) lines. In these time snapshots, the quark core surface, where $X_{quark} = 1$, is located at $r \sim 6 \times 10^5$ cm, without changing its location. Meanwhile, the shock front propagates from $r \sim 6 \times 10^5$ cm at $t_{p2b} = -0.01$ ms to $\sim 9 \times 10^5$ cm at $t_{p2b} = 0.05$ ms. It is obvious that ω_{BV} in front of the second bounce shock is negative, which indicates a convectively unstable region according to the Ledoux criterion, as well as high angular frequencies, reaching $|\omega_{BV}|/2\pi \sim 10$ ms^{-1}. The convectively unstable region corresponds to the region with a steep negative lepton number gradient (see Y_e profile in Figure 5) as well as to the entropy jump at the second bounce shock surface. Due to having such a high ω_{BV}, the convective motions can fully develop behind the shock even within a millisecond and be the seed of the subsequent Rayleigh–Taylor instability. Furthermore, in the convectively stable region (i.e., $\omega_{BV} > 0$) between the quark core and the second bounce shock surface (6×10^5 cm $\lesssim r \lesssim 9 \times 10^5$ cm at $t_{p2b} = 0.05$ ms), we see the angular frequencies (or the so-called "plume frequencies" (Murphy et al. 2009)) reaching $\omega_{BV}/2\pi \sim$ a few kHz. This buoyancy frequency can reasonably explain the GW frequency at the second bounce, which will be discussed in the next section.

4. GW and Neutrino Emission

In this section, we discuss the impact of the hadron–quark phase transition on the emission of gravitational waves and neutrinos. In Figure 10, we plot gravitational waveforms and their spectrogram for all models. Here, we show only a nonvanishing component $A_+ = Dh_+$ observed along the equatorial plane that is perpendicular to the symmetric axis. D and h_+ are the source distance and gravitational wave strain, respectively. The value of h_+ is evaluated from a standard quadrupole formula (Shibata & Sekiguchi 2003; Kuroda et al. 2014).

A common feature seen among all models is relatively large GW amplitudes, observed after the first core bounce until $t_{pb} \sim 50$ ms. These GWs are emitted from the post-bounce convective motions and their amplitudes reach ∼20–50 cm. Afterward, the gravitational waveforms show various features depending on the progenitor mass. Our least massive star, *z*9.6, which is the NDE model and experiences the runaway explosion at around $t_{pb} \sim 100$ ms (see Figure 4), shows a considerable subsidence of GWs. Using a similar progenitor mass model of $9\,M_\odot$, Vartanyan et al. (2019) and Andresen et al. (2021) also reported the subsidence of GWs. Those authors found that it is due to a termination of mass accretion. Furthermore, the waveform is quite similar to that of the 2D relativistic model of Müller et al. (2013).

Another NDE model, *s*11.2, presents continuous GW emission even after the shock front exceeds 10^8 cm at $t_{pb} \sim 500$ ms. Furthermore, the waveform seems to show an increasing frequency, which can be indeed confirmed from the spectrogram in the lower panel. The peak frequency concentrates around ∼200 Hz at $t_{pb} = 200$ ms and is increasing with time. Such a ramp-up feature of the GW frequency is widely seen in CCSN models (Murphy et al. 2009; Müller et al. 2013; Kuroda et al. 2016a; Vartanyan et al. 2019; Mezzacappa et al. 2020; Shibagaki et al. 2021) and may come from the g/f-mode oscillation of the nonrotating PNS (Morozova et al. 2018; Torres-Forné et al. 2019; Sotani & Takiwaki 2020) or perhaps PNS convection (Mezzacappa et al. 2020). In the late post-bounce phase $t_{pb} \gtrsim 600$ ms, the spectrogram shows a wideband emission ranging from 300 Hz to a few kHz. Since we use a simple short-time Fourier analysis to obtain the spectrogram, we need to apply sophisticated analysis methods, such as S-method (Kawahara et al. 2018), the Hilbert–Huang transform (Takeda et al. 2021), or nonharmonic analysis (Yanagisawa et al. 2019) to determine a more detailed peak frequency.

Regarding the PDE model *s*50, the ramp-up feature can also be seen in the first ∼200 ms after the bounce. It is remarkable that the ramp-up mode is showing a more rapid evolution in its peak frequency than that in *s*11.2. At $t_{pb} \sim 180$ ms, the peak frequency appears at ∼500 Hz, which is significantly higher than ∼200 Hz for *s*11.2. The higher frequency in model *s*50 is

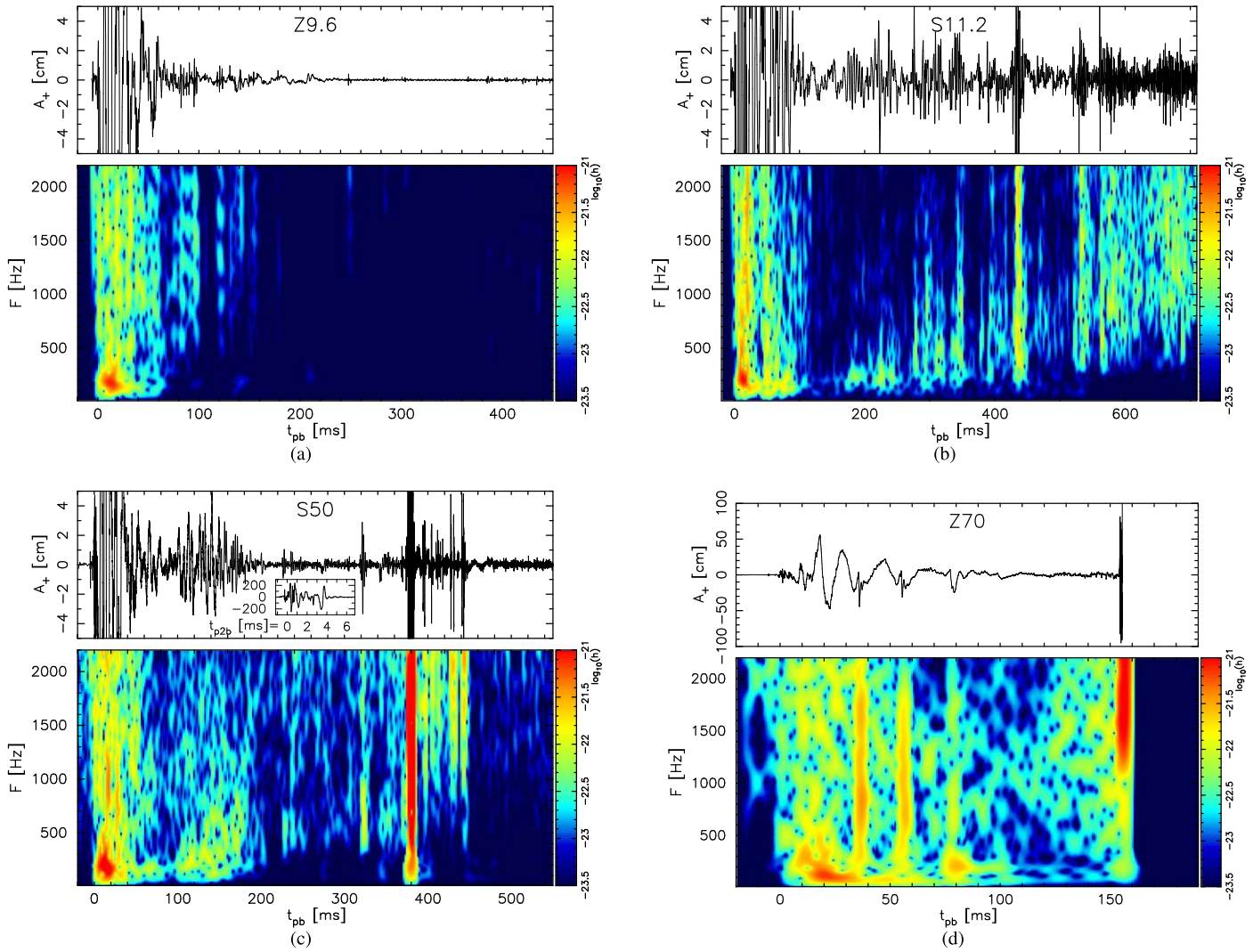

Figure 10. Gravitational waveform A_+ (top panels) and the corresponding spectrogram (bottom panels) for all models, labeled in each top panel. Here, we show only the nonvanishing component in axisymmetric profile $A_+ \equiv Dh_+$ observed along the equatorial plane, which is perpendicular to the symmetric axis. The spectrogram is obtained by short-time Fourier transform. D and h_+ are the source distance and gravitational wave strain, respectively, where the latter is calculated from a standard quadrupole formula. For $s50$, we also plot a magnified view of the gravitational waveform with respect to the second bounce time in the inner mini-panel of the top panel.

simply due to a higher compactness of the PNS (see Table 1) and its higher g/f-mode oscillations. From $t_{\rm pb} \sim 200$ ms to the second bounce time $t_{\rm pb} \sim 380$ ms, the GW emission shows a quiescent phase, during which the amplitudes are basically less than $\sim$1 cm. Such a quiescent phase can also be seen in our most massive star case, $z70$, at $t_{\rm pb} \gtrsim 100$ ms. In both models, the quiescent phase roughly corresponds to the period when the shock gradually recedes (Figure 4). Although this paper does not aim to clarify the physical mechanism of the quiescent phase, we speculate that the rapid shock recession may suppress the convective motions, which usually excite the PNS core g/f-mode oscillations. As a consequence, the weaker GWs are observed. However, in the full 3D models, the situation may drastically change, as another degree of spatial freedom allows for the development of the standing accretion shock instability (SASI) (Blondin et al. 2003). In such models, the more compact PNS core is more susceptible to the SASI development. The SASI activity can then imprint its feature in the emitted GW with sizeable amplitudes, typically in the low frequency range of $\sim$100–200 Hz (Kuroda et al. 2016a; Andresen et al. 2017; Vartanyan et al. 2019; Mezzacappa et al. 2020; Shibagaki et al. 2021).

The quiescent phase is disrupted by the hadron–quark phase transition. Both models $s50$ and $z70$ experience the second collapse at $t_{\rm pb} \sim 380$ ms and $t_{\rm pb} \sim 155$ ms, respectively. Although $z70$ immediately forms a BH, both models produce a quark core at their center and exhibit core bounce and a subsequent ring-down phase. In the inset of the upper panel for $s50$, we show a magnified view of the waveform at the second bounce. The x-axis measures the time relative to the second bounce in millisecond. The GW amplitudes reach $A_+ \sim 250$ cm, and the strong emission lasts about 4 ms after the second bounce time. Its burst-like feature results in a wideband emission, ranging from $\sim$500 Hz to beyond 2.5 kHz, where the latter value corresponds to the Nyquist frequency of our sampling rate of 5 kHz. Such high frequencies are comparable to typical frequencies of the convection motions behind the second bounce shock as shown in Figure 9, where we see $|\omega_{\rm BV}| \sim$ a few kHz at 6×10^5 cm $\lesssim r \lesssim 9 \times 10^5$ cm. Therefore, these high-frequency GWs could be an outcome of these convection

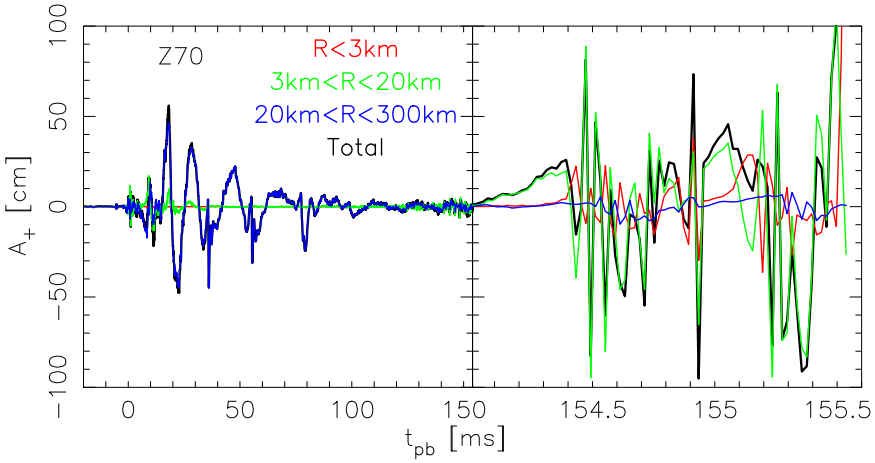

Figure 11. GW amplitudes A_+ for the model $z70$ contributed from different spherical shells: innermost region with $r \leqslant 3$ km (red line), 3 km $< r \leqslant 20$ km (green line), and 20 km $< r \leqslant 300$ km (blue line). Black line indicates the total gravitational waveform.

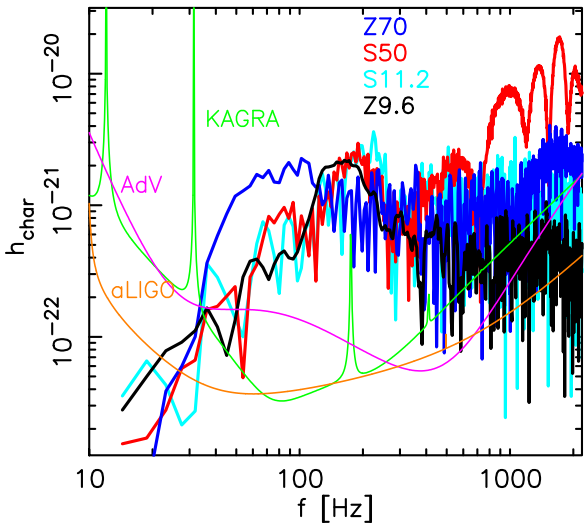

Figure 12. Characteristic GW spectral amplitudes for all models assuming a source distance of 10 kpc. The noise amplitudes of aLIGO (orange line), AdV (magenta line), and KAGRA (green line) are plotted as references. Note that, since the Nyquist frequency is 2500 Hz, we show only $f \lesssim 2000$ Hz.

motions induced by the hadron–quark phase transition. During the post-second-bounce phase in $s50$, the GWs show a high-frequency emission at the range of $\gtrsim$1 kHz and they subside after $t_{\rm pb(p2b)} \sim 460(80)$ ms. The maximum amplitude and the duration time of the strong emission are comparable to those in Zha et al. (2020).

Regarding the BH formation model $z70$, it also shows a high peak frequency $\gtrsim$1 kHz and amplitudes reaching $A_+ \sim 100$ cm. In contrast to the full 3D BH formation models (Kuroda et al. 2018; Shibagaki et al. 2021), whose GW waveforms are contaminated by the low-frequency SASI modes, the GW signal at the BH formation shows a higher peak frequency (this could be consistent with Sotani & Sumiyoshi (2019, 2021)). This is not only due to the absence of significant SASI motions but also to the quark core formation and its oscillation. We crudely check if the GW emissions prior to the BH formation actually emanate from outside the apparent horizon. In Figure 11, we show the GW amplitudes A_+ for model $z70$ contributed from different spherical shells: the innermost region with $r \leqslant 3$ km (red line), 3 km $< r \leqslant 20$ km (green), and 20 km $< r \leqslant 300$ km (blue). A black line indicates the total gravitational waveform. To plot the figure, we simply divide the computational domain into several spherical shells, calculate the contained mass quadrupole moment inside each shell, and derive the gravitational wave strain.

One can see that the blue line overlaps with the black one in most of the post-bounce phase up to $t_{\rm pb} = 150$ ms. This indicates that the dominant contribution to the total GW is coming from the post-shocked region, roughly corresponding to the region with 20 km $< r \leqslant 300$ km. Meanwhile, the inner region with $r \leqslant 20$ km shows essentially no GW emission except during the initial post-convection phase ($t_{\rm pb} \lesssim 30$ ms). However, just prior to the second collapse ($t_{\rm pb} \geqslant 154$ ms, i.e., less than $\sim$1 ms until the BH formation), the dominant contribution is from $r \leqslant 20$ km. At this moment, the quark core is already formed. Although the contribution from the innermost region with $r \leqslant 3$ km is not negligible (see the red line), the majority comes from outside of the apparent horizon, i.e., 3 km $< r \leqslant 20$ km. Here, we note that the circumferential radius of AH is $\sim$2.29 km at the final simulation time. Therefore, the signal of the QCD phase transition could be imprinted into the emanated GWs, even in the failed CCSN models. However, we stress that the gravitational waveform can greatly change in the full 3D models and also that the gravitational wave should be evaluated more precisely by the gauge-invariant method, especially in such a model on a highly curved spacetime.

To discuss the detectability of the GW signals, we show the GW spectral amplitudes for all models in Figure 12, assuming a source distance of 10 kpc, together with the sensitivity curves of the advanced LIGO (aLIGO), advanced VIRGO (AdV), and KAGRA (Abbott et al. 2018). The common feature seen among the models is a spectral peak appearing in a relatively low frequency range of $\sim$100–200 Hz. From the spectrogram in Figure 10, such low-frequency GWs are emitted mainly by convection motions in the post-bounce phase. Our most massive progenitor model, $z70$, shows a relatively lower peak frequency compared to the other models appearing at $50 \lesssim f \lesssim 100$ Hz. This can be explained by the less compact PNS for model $z70$, although the PNS soon becomes more compact than the rest of the models, due to a higher mass accretion rate.

Once the initial convection motion ceases, the GW frequency increases with time. While $z9.6$ has only one spectral peak at $f \sim 150$ Hz, due to a considerable subsidence of

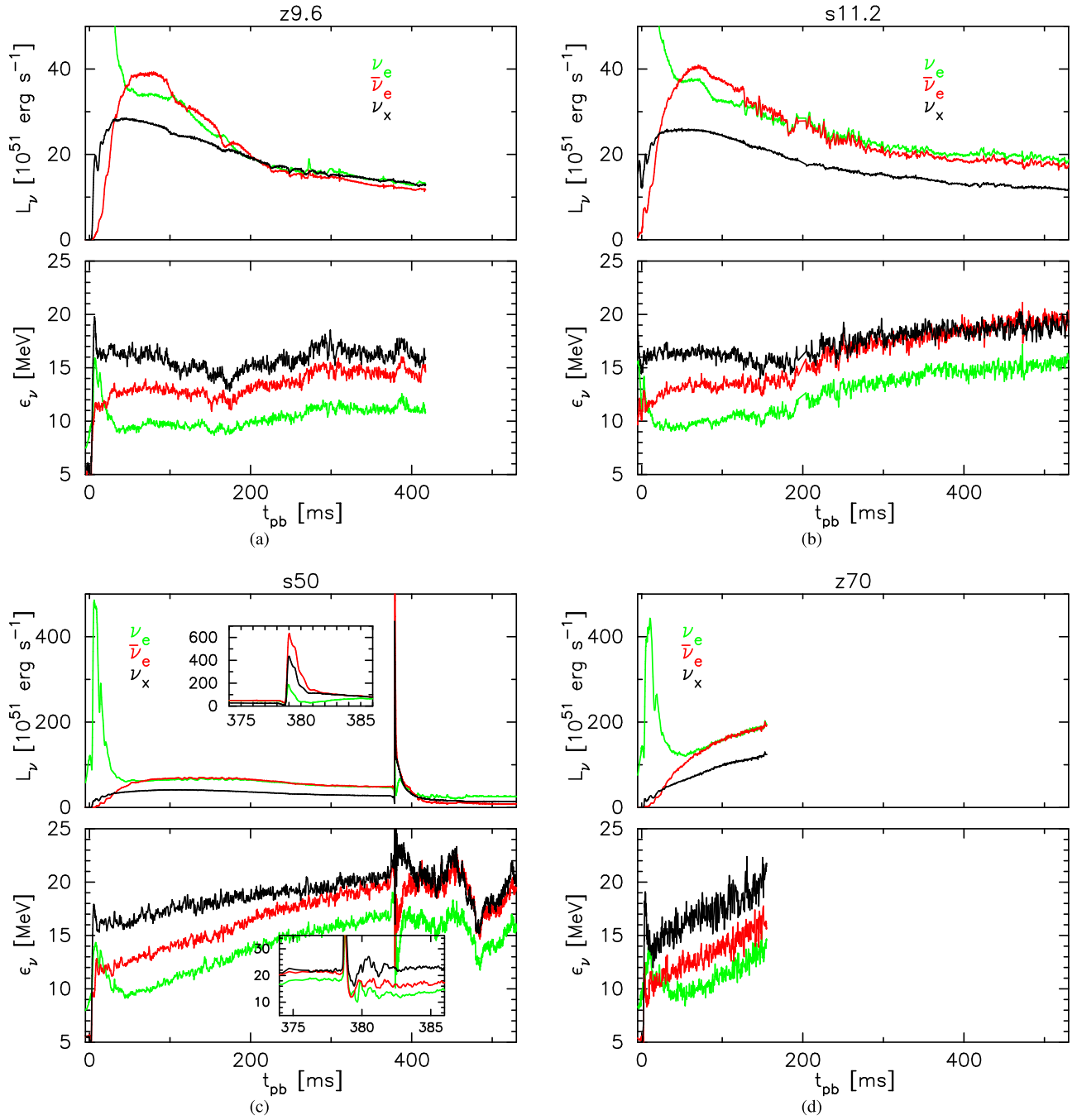

Figure 13. Post-bounce evolution of the neutrino luminosities (top panels) and mean neutrino energies (bottom panels) for all models. Green, red, and black lines correspond to ν_e, $\bar{\nu}_e$, and ν_x, respectively. For $s50$, the inlays show the second burst.

GWs after $t_{pb} \gtrsim 100$ ms, the other models exhibit a broadband emission ($s11.2$) extending from $\sim$200 Hz to $\gtrsim$1000 Hz, or rather, a double-peaked feature ($s50$ and $z70$). The high-frequency emission seen in model $s11.2$ has an amplitude $h_{\rm char} \sim 2 \times 10^{-21}$ that is nearly comparable with that of the low-frequency emission. It is emitted in the late post-bounce phase, $t_{pb} \gtrsim 300$ ms from Figure 10(b), and mainly originates from the oscillation of a contracting PNS or its convection (which is still under debate). Here, $s50$ and $z70$ also have a high-frequency spectral peak appearing at $\sim$1700 Hz. From Figure 10, such a high-frequency emission occurs during the second collapse and is associated with the hadron–quark phase transition and its subsequent convection motions as already explained (see also Figure 9). The amplitude at $f \gtrsim 1000$ Hz in model $s50$ is well above the sensitivity curves of the current-generation GW detectors, and could be detectable if the source is located within our Galaxy. The present GW analysis for $s50$ is in qualitative agreement with the results reported by Zha et al. (2020), in particular the locations of the secondary peaks in excess of 1000 Hz, which are related to the dynamics of hadron–quark phase transition.

Figure 13 presents the neutrino luminosities and mean energies for all models.[6] All quantities are evaluated at a

[6] We have checked the reliability of current neutrino transport method in the Cartoon coordinates using the standard neutrino opacity set, which is summarized in Appendix B.

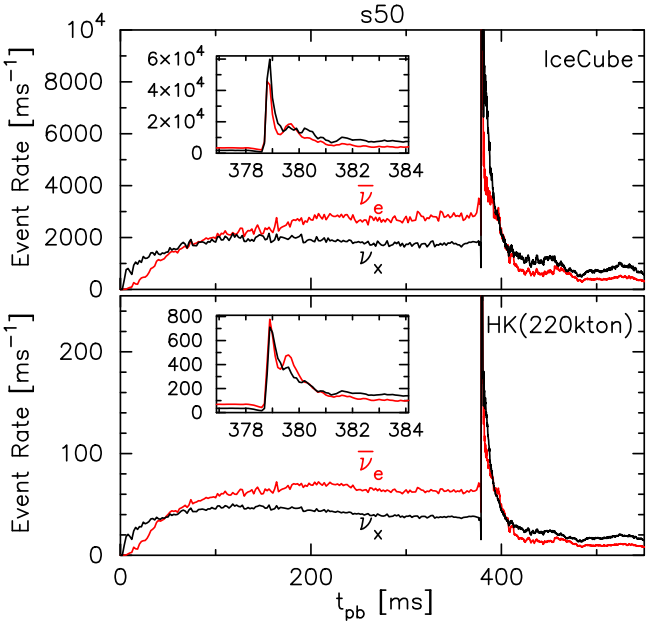

Figure 14. Neutrino detection rate of IceCube (top panel) and HK (bottom panel) as a function of time after bounce for model *s*50 observed at 10 kpc. The red and black lines are for $\bar{\nu}_e$, assuming no flavor conversion, and for $\bar{\nu}_x$, assuming complete flavor conversion, respectively. The inlays show the second burst.

distance of $r = 400$ km. Compared with the full GR 2D models in Müller & Janka (2014), the less massive progenitor models *z*9.6 and *s*11.2 show very similar neutrino profiles. We note that the detailed neutrino opacities are different between this study and theirs. The neutrino luminosities of all flavors overlap each other at $t_{\rm pb} \gtrsim 200$ ms in model *z*9.6. The neutrino mean energies show only a slight increase with time, which indicates that the PNS core does not shrink significantly in this model. At $t_{\rm pb} = 400$ ms, $L_{\nu_e,\bar{\nu}_e,\nu_x}$ become $\sim 1.2 \times 10^{52}$ erg s^{-1} and mean energies reach $\varepsilon_\nu \sim 11$, 14, and 16 MeV for ν_e, $\bar{\nu}_e$, and ν_x, respectively. In *s*11.2, the accretion luminosities peak at around $t_{\rm pb} \sim 90$ and reach $L_{\nu_e,\bar{\nu}_e} \sim 4 \times 10^{52}$ erg s^{-1} and $L_{\nu_x} \sim 2.5 \times 10^{52}$ erg s^{-1}. Afterward, they show a decreasing trend. The mean neutrino energies become higher with time, and $\varepsilon_{\bar{\nu}_e}$ reaches nearly the same value as ε_{ν_x} at $t_{\rm pb} \gtrsim 300$ ms. All of these features seen in both *z*9.6 and *s*11.2 are roughly in good agreement with those in Müller & Janka (2014).

*s*50 shows a quite remarkable feature in association with the hadron–quark phase transition. After the first bounce, L_{ν_e} and $L_{\bar{\nu}_e}$ have almost the same values at $t_{\rm pb} \gtrsim 60$ ms, while L_{ν_x} shows a value of nearly half of the electron-type (anti-)neutrino luminosities. When the second collapse is initiated, the neutrino luminosities of all flavors drastically increase. From the inset panel, we see that $L_{\bar{\nu}_e}$ and L_{ν_e} show the highest and lowest luminosity, respectively, and such a hierarchy is consistent with Fischer et al. (2020). The hierarchy can be explained by the neutron-rich environment through which the shock propagates. As we have explained in Figure 5, the shock is generated beneath the Y_e trough and propagates through the neutron-rich environment. Therefore, abundant electron-type antineutrinos are produced via the inverse beta decay process, leading to the highest $L_{\bar{\nu}_e}$. The peak luminosity of $L_{\bar{\nu}_e} \sim 6 \times 10^{53}$ erg s^{-1} at the second bounce is on nearly the same order as that of $L_{\nu_e} \sim 5 \times 10^{53}$ erg s^{-1} at the first bounce. Such a feature is also reported in Fischer et al. (2020).

The mean neutrino energies in our most compact model, *z*70, show the fastest increase. This is due to it having the most rapid PNS contraction among the models, and consequently the hottest PNS core (Liebendörfer et al. 2004; Sumiyoshi et al. 2007). Shibagaki et al. (2021) reported the neutrino luminosities for the same $70\,M_\odot$ progenitor model with different nuclear EOS and neutrino opacities. Compared to their results, the neutrino luminosities show slightly higher values of ∼20% in all flavors. The neutrino signal associated with the QCD phase transition is not plotted in the figure. This is because we evaluate the neutrino flux at $r = 400$ km, and the simulation stops before the neutrino burst reaches that sphere.

Finally, we discuss the detectability of the second neutrino burst in association with the hadron–quark phase transition for model *s*50. Figure 14 illustrates the neutrino detection rate of IceCube (top panel) and HK (bottom panel) as a function of post-bounce time for model *s*50 observed at 10 kpc. We evaluate the event rates of each model for two neutrino detectors: IceCube (Abbasi et al. 2011, Salathe et al. 2012) and Hyper-Kamiokande (Abe et al. 2011; Hyper-Kamiokande Proto-Collaboration et al. 2018, hereafter HK). The main channel in these detectors is of anti-electron neutrino ($\bar{\nu}_e$) with inverse-beta decay. For simplicity, we take into account only this channel to evaluate the event rates. We assume that the neutrino energy spectrum is a Fermi–Dirac distribution (see Lund et al. (2010) and Takiwaki & Kotake (2018) for more detail). Furthermore, in the evaluation, we consider two extreme cases: one in which all $\bar{\nu}_e$ emitted from the source reach the detectors without neutrino flavor conversion and cause the signal at the detectors (red lines in the figure); and another in which all $\bar{\nu}_x$ (identical to ν_x in this study) emitted from the source are completely swapped by $\bar{\nu}_e$ and cause the signals (black lines).

From the plot, we find that, during the first ∼50 ms after bounce, the $\bar{\nu}_x$ signal shows a larger detection rate for both detectors. Afterward, the $\bar{\nu}_e$ signal becomes stronger than that of $\bar{\nu}_x$. After $t_{\rm pb} \sim 100$ ms, both signals show nearly constant values until the onset of the second collapse. Such features are consistent with previous normal CCSN models (Tamborra et al. 2013; Nagakura et al. 2021b). Once the second collapse takes place, the signals become approximately 30 times stronger than the values before the second collapse. The peak values for both $\bar{\nu}_e$ and $\bar{\nu}_x$ signals reach nearly the same value of ∼5000 ms^{-1} (IceCube) and ∼700 ms^{-1} (HK). Fischer et al. (2018) reported the number of expected neutrino events in the Super-Kamiokande (SK) detector of ∼100 with 2 ms bins from the second neutrino burst event, assuming a source distance of 10 kpc. Concerning the fiducial volume of HK, which is approximately 10 times larger than that of SK, our expected event rate ∼700 ms^{-1} in HK can be converted to ∼140 signals with 2 ms bins, which is in line with that of Fischer et al. (2018).

5. Summary and Discussion

In this study, we have presented possible effects of the phase transition from hadronic matter to quark matter in CCSNe. For this purpose, we have performed 2D axisymmetric numerical simulations of the core collapse of massive stars with $9.6\,M_\odot$, $11.2\,M_\odot$, $50\,M_\odot$, and $70\,M_\odot$. Our core-collapse supernova model is based on numerical relativity, which solves the general relativistic neutrino radiation hydrodynamics equations together with the two-moment (M1) neutrino transport

equations of Kuroda et al. (2016b). We use up-to-date neutrino opacities following Kotake et al. (2018). We employed the hybrid EOS DD2F–RDF 1.2 of Fischer et al. (2018) and Bastian (2021), which considers a first-order hadron–quark phase transition.

Our results demonstrate a diversity of post-bounce evolutions depending on the progenitor. We confirm that low- and intermediate-mass progenitors, examined using the examples of a low-metallicity model with ZAMS mass of $9.6\,M_{\odot}$ and a solar-metallicity model with ZAMS mass of $11.2\,M_{\odot}$, belong to the class of core-collapse supernova explosion driven by the neutrino-heating mechanism. The latter one is aided by the presence and development of convection. Both neutrino-driven explosion models are in qualitative agreement with previous studies, e.g., in terms of the explosion dynamics as well as the diagnostic explosion energy obtained. None of these models reach the conditions required for the hadron–quark phase transition, prior to the onset of the supernova explosion. In contrast, the more massive progenitors explored with ZAMS mass of $50\,M_{\odot}$ of solar metallicity and an extremely metal-poor star with ZAMS mass of $70\,M_{\odot}$ both undergo the phase transition during the post-bounce mass accretion phase. However, an explosion is obtained only for the $50\,M_{\odot}$ model, while for the $70\,M_{\odot}$ model we observe a failed explosion and black hole formation instead. This is related to the maximum mass of the DD2F–RDF 1.2 hybrid EOS, which the latter one exceeds at the onset of the hadron–quark phase transition. In contrast, therefore, for the $50\,M_{\odot}$ model we report the formation and propagation of a second shock wave as a direct consequence of the hadron–quark phase transition, which determines the onset of the supernova explosion, in qualitative agreement with the results reported by Fischer et al. (2018) and Fischer et al. (2020). Nevertheless, the as-yet incompletely understood question regarding the dependence on metallicity, preliminarily addressed in Fischer (2021), remains to be explored in a more systematic study.

Our finding inherent to the multi-D nature is the strong RT mixing. In the context of CCSNe, the potential region of development of the RT mixing is usually distant from the PNS, e.g., the interface between CO core and He layer (Wongwathanarat et al. 2015), which is located at $r \gtrsim 10^{9-10}$ cm depending on the progenitor model. However, because of the shallow density profile in $s50$, the RT mixing can develop even at a distance of $r \sim 10^{8}$ cm. Because of the short distance, the RT mixing can develop in the early post-explosion phase of a few tens of ms after the explosion onset has been launched, in terms of the initial propagation of the second shock wave. A combination of the PDE and a prompt development of the RT mixing might have an influence on the nucleosynthetic yields previously reported in Fischer et al. (2020).

Furthermore, we discussed possible effects of the hadron–quark phase transition on the multi-messenger observables, gravitational waves, and neutrinos. For the less massive progenitor models, $s9.6$ and $s11.2$, we confirm commonly found features in their GW signals: $z9.6$ showed a subsidence of GW emission, once it entered a runaway explosion phase at $t_{\rm pb} \gtrsim 200$ ms, and $s11.2$ exhibited a rather constant GW emission even after its explosion, though the peak frequency increased with time in association with the PNS contraction. The massive progenitor stars $s50$ and $z70$ display a quiescent phase for GW emission once their standing shock front starts to recede. However, in full 3D models, the SASI phase could arise in this period and contribute to the GW emission. The contribution can be sufficient to produce sizeable GWs, according to the previous 3D studies (e.g., Kuroda et al. 2016a). At the second bounce in $s50$, ring-down of the quark core produces strong and high-frequency GWs, with their amplitudes and typical frequencies exceeding Dh ~ 250 cm and 1 kHz, respectively. Because the Brunt–Väisälä frequencies behind the second bounce shock reach a few kHz, the high-frequency GWs could be an outcome of these convection motions (see also the supplemental material of Zha et al. (2020), for the relation between the convection motions behind the second bounce shock and typical GW frequencies.). Although their typical frequency appears to be in the kHz range, which is out of the best sensitivity of current ground-based gravitational wave detectors, their signal is strong enough to be detected, if the source is located at 10 kpc. Even in the failed explosion case, $z70$, the region outside the apparent horizon contributes significant GW emission. Thus, we can expect that the signal of a hadron–quark phase transition might be imprinted in GWs even in the failed CCSNe, although the detailed waveform should be examined in full 3D models, considering the SASI development.

Concerning the neutrino profiles, the neutrino luminosity and mean energy of all flavors have shown quite reasonable values in models $z9.6$ and $s11.2$ as compared with previous studies (e.g., with the 2D relativistic models of Müller & Janka (2014)), since these two less-massive progenitor models do not undergo the hadron–quark phase transition during our simulation time. In $s50$, on the other hand, we have observed the second neutrino burst when the second core bounce takes place. In contrast to the first bounce, the electron-type antineutrino luminosity $L_{\bar{\nu}_e}$ exhibits the highest luminosity among the flavors. This is because the quark core bounce occurs below the Y_e trough, and the shock propagates through the neutron-rich environment. Therefore, the inverse beta decay becomes the dominant reaction process and produces numerous electron-type antineutrinos. The hierarchy seen in the second neutrino burst is consistent with previous studies (Fischer et al. 2018; Zha et al. 2020).

Recently, long-time 2D SN simulations, longer than several seconds in 2D (see Müller 2015; Nakamura et al. 2019; Burrows & Vartanyan 2021; Nagakura et al. 2021a), and even in 3D by Bollig et al. (2021), have become computationally feasible. Because of our short simulation times, the diagnostic explosion energies of models $z9.6$ and $s11.2$ do not reach energy saturation. According to Müller (2015), the energy saturation can be reached after $\sim$5 s for model $s11.2$. Such long-time simulations are necessary to discuss the diagnostic explosion energy, as well as the final property of remnant star. It is worth mentioning that the inclusion of the progenitor's precollapse inhomogeneities in the burning shells (Yoshida et al. 2019, 2020, 2021; Yadav et al. 2020) has been pointed out to make the underpowered explosion more energetic (Müller & Janka 2015; Bollig et al. 2021). Starting from the multi-D progenitors, we have to study how the multi-D hydrodynamic motions in the pre-explosion phase result in the multi-messenger signals up to the late explosion phase (see previous attempts in Nakamura et al. (2019), Nagakura et al. (2021a), and Witt et al. (2021)). Though this is not an easy task, this may be the only promising method available, and one we should be pursuing in order to enhance the predictive power of CCSN multi-messenger signals as quantitatively as possible.

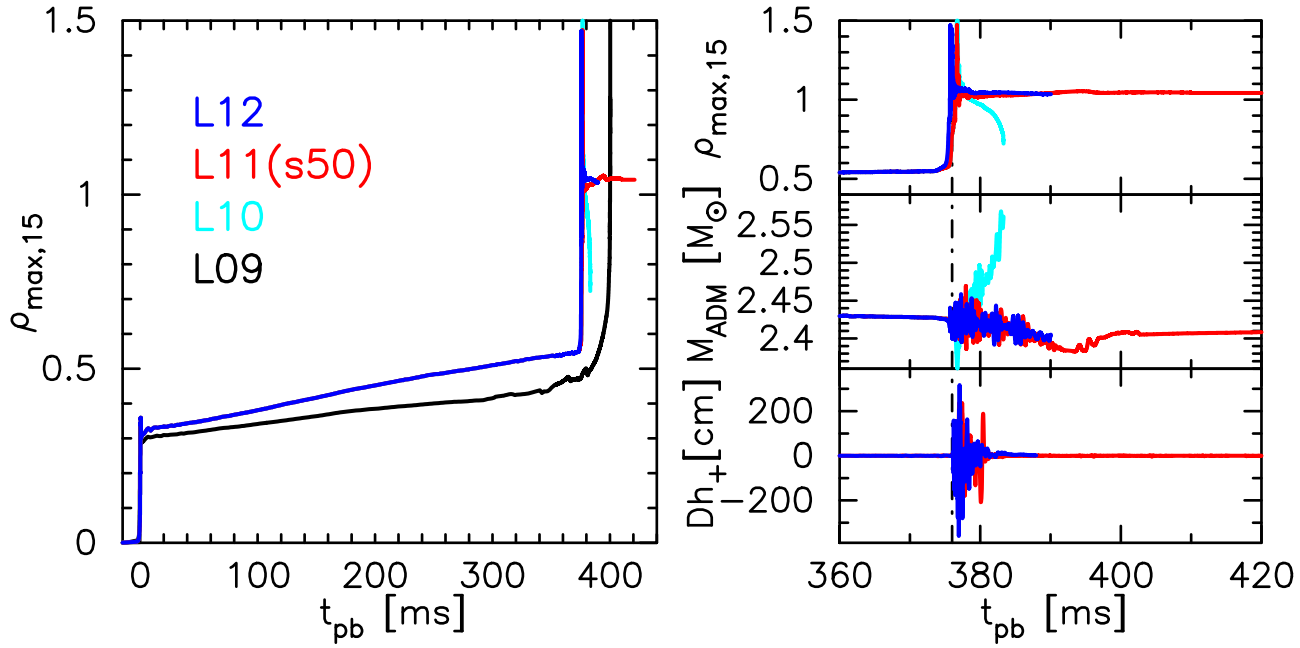

Figure 15. Left panel: Evolution of the maximum density $\rho_{max,15}(\equiv\rho_{max}/10^{15})$ for four cases *L*09–*L*12 (see text for their numerical setup). Right panel: Zoom-in for the evolution of the maximum density $\rho_{max,15}$ (top panel) and ADM mass M_{ADM} (bottom panel) for *L*12 (blue line), *L*11 (red line), and *L*10 (light blue), focusing on the post-second-bounce phase. The vertical dotted–dashed lines indicate when we raise the maximum refinement level from $L_{max} = 10$ to 11.

We thank the referee Shuai Zha for clarifications that improved this article. We are also grateful to N. U. Bastian for providing (extending) the EOS table, which is readily employed in the multi-D CCSN simulations. T.K., T.T., and K.K. are thankful to H. Ookawa for helpful discussions in developing the apparent horizon finder in this work. Numerical computations were carried out on Cray XC50 at CfCA, NAOJ, and also on Sakura and Raven at the Max Planck Computing and Data Facility. T.F. acknowledges support from the Polish National Science Center (NCN) under Grant No. 2019/33/B/ST9/03059. This work was supported in part by the Japan Society for the Promotion of Science (JSPS) KAKENHI Grant Numbers JP17H06357, JP17H06364, JP18H01212, JP21H01088. K.K. was supported by the Research Institute of Stellar Explosive Phenomena at Fukuoka University and the associated project (No.207002).

Appendix A
Spatial Resolution Test

In this appendix, we show the spatial resolution dependence of the post-bounce PNS evolution, to demonstrate that the currently used spatial resolution is adequate to follow the quark core evolution. For that purpose, we perform four CCSN simulations "*L*09–12" with different spatial resolutions. The integer after *L* represents the maximum refinement level set for the nested structure, e.g., *L*10 corresponds to a model with a maximum refinement level of $L_{max} = 10$. The central grid width is halved by raising the level by one. As a result, the central numerical grid width achieves ∼460, 230, 115, and 57 m for *L*09, *L*10, *L*11, and *L*12, respectively. However, we do not run these models with a static nested structure from initial conditions; instead, we raise the level of nested structure depending on the value of maximum rest-mass density as follows. In *L*09 and *L*10, we do not change the maximum refinement level throughout the calculations. These models are calculated to see the resolution dependence mainly on the PNS contraction phase, including the second collapse time. In *L*11 and *L*12, we restart *L*10 shortly before its maximum rest-mass density ρ_{max} reaches 8×10^{14} g cm^{-3}. Then we raise the level to $L_{max} = 11$ once ρ_{max} exceeds 8×10^{14} g cm^{-3}. Furthermore, in *L*12, we again raise the level to $L_{max} = 12$ when ρ_{max} exceeds 9×10^{14} g cm^{-3}. *L*11 is identical to the model *s*50 discussed in the main text, and *L*10–12 are calculated to check the resolution dependence, particularly focusing on the quark core formation and subsequent evolution phase.

In the left panel in Figure 15, the maximum density evolution is plotted for four cases *L*09–*L*12. In the right panel, we show the maximum density (top), ADM mass (middle), and GW amplitudes A_+ (bottom) for *L*12 (blue line), *L*11 (red line), and *L*10 (light blue), focusing on the post-second-bounce phase. As for the gravitational waveform, we plot it only for *L*11 and *L*12. We first check the impact of numerical resolution on the PNS contraction phase and also on the second collapse time. Since there is essentially no difference in the second collapse time among the three models *L*10–*L*12, here we compare *L*12 (blue) and *L*10 (black) in the left panel. The finest numerical grid in these two models is ∼230 m (blue) or ∼450 m (black) during the PNS contraction phase ($t_{pb} \lesssim 350$ ms). From the left panel, the black line systematically shows a smaller maximum density compared to that of *L*12 (note that the blue, red, and light blue lines are identical when $\rho_{max,15} < 0.8$). Although the difference already appears at just after the first bounce, we also find that the central entropy secularly increases in *L*09 (not shown in the figure). This is due to the numerical dissipation in lower-resolution model *L*09. Therefore, the maximum density in *L*09 shows a smaller value throughout the PNS contraction phase. However, the second collapse times in *L*10–12 and *L*09 exhibit a rough convergence, with only a ∼20 ms difference between the red and black lines. Thus, we can say that, for the PNS contraction phase, a rough numerical convergence is achieved for a grid width smaller than ∼450 m.

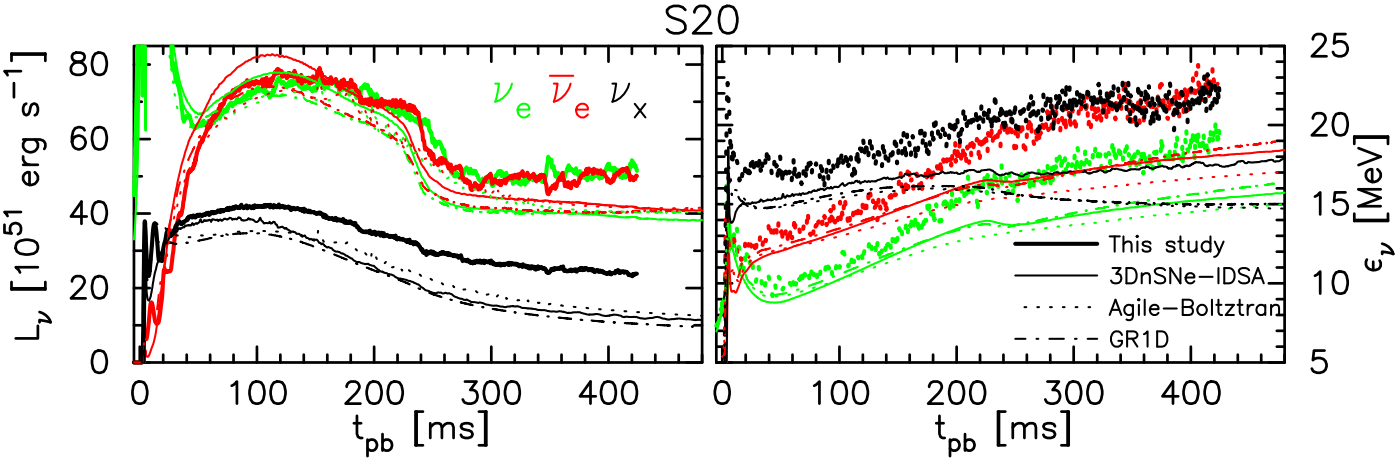

Figure 16. Post-bounce evolution of the neutrino luminosities (left panel) and mean neutrino energies (right panel) for the solar metallicity, nonrotating 20 $M_\odot$ progenitor star from Woosley & Heger (2007). The latter is identical to the one used in a global comparison of CCSNe simulations reported by O'Connor et al. (2018). The neutrino opacity is the same as was used in O'Connor et al. (2018). Green, red, and black lines correspond to ν_e, $\bar{\nu}_e$, and ν_x, respectively. (Reply to Q14) Thick lines are results of this study, while thin, dotted, and dashed–dotted lines are results obtained using the 3DNSNE-IDSA code (Takiwaki et al. 2016), AGILE-BOLTZTRAN code (Liebendörfer et al. 2004), and GR1D code (O'Connor 2015), respectively.

Next, we compare *L*10, *L*11, and *L*12, focusing on the numerical convergence after the second core bounce. From top right panel, it is obvious that the maximum density drastically decreases after the second core bounce in *L*10 (light blue). At the same time, the ADM mass significantly increases, and it does not settle into a new quark core branch as *L*11 does. This is because the lower-resolution model *L*10 suffers from a severe numerical dissipation and the quark core seems to be artificially gravitationally unbound. From a comparison between *L*11 and *L*12, though we cannot follow a long-time evolution for the highest-numerical-resolution model *L*12, we see an apparent convergence in the post-second-bounce evolution at least during the first ∼15 ms. Both the maximum rest-mass density and the ADM mass are exhibiting consistent evolutions. In addition, from the bottom right panel, the strong GW emissions associated with the second bounce are roughly converged among these two models. Indeed, the observed maximum amplitude $|A_+| \sim 300$ cm and duration time of ∼5 ms are comparable in *L*11 and *L*12. Because the emission considered here is due to stochastic motions during the ring-down phase, a convergence in the maximum amplitude and duration time is sufficient for the spatial resolution check. From these comparisons, we conclude that a resolution of ∼110 m used in *L*11(*s*50) is required in order to adequately resolve the quark core evolution.

Appendix B
Test for the Neutrino Transport in a Mixed Frame of Cylindrical and Cartoon Coordinates

This appendix is devoted to testing our neutrino transport in a mixed frame of cylindrical and Cartoon coordinates, in which all hydrodynamical and neutrino-radiation quantities, as well as the metric variables, are not evolved straightforwardly as in the Cartesian coordinates used in our previous studies (e.g., Kuroda et al. 2016b). To this end, we perform the same CCSN simulation reported by O'Connor et al. (2018), follow the collapse of the solar metallicity, nonrotating 20 $M_\odot$ star taken from Woosley & Heger (2007), and compare the neutrino profiles. Furthermore, the neutrino opacity is also consistent with O'Connor et al. (2018) and uses the baseline set of Bruenn (1985) including the Brehmsstrahlung of Hannestad & Raffelt (1998). There are 20 energy bins, which logarithmically cover the region of 0–300 MeV. One of the major differences from O'Connor et al. (2018) is the spherically symmetric property, which we cannot take into account in the Cartoon coordinates based numerical code. We also note that the presented model is calculated via numerical relativity and thus might have some inherent differences from that in O'Connor et al. (2018). Therefore, in the late post-bounce phase, when the convection motions become dominant, our neutrino profiles show results different from those in O'Connor et al. (2018). In Figure 16, we use thick lines to plot neutrino luminosities (left) and mean neutrino energies (right) extracted at a radius of $r = 400$ km. In addition, we plot three reference cases obtained by using the following codes: 3DnSNe-IDSA (Takiwaki et al. 2016) (thin line), AGILE-BOLTZTRAN (Liebendörfer et al. 2004) (dotted line), and GR1D (O'Connor 2015) (dashed–dotted line). The data for these reference cases were downloaded from the publisher site of O'Connor et al. (2018).

We first explain the comparison of the neutrino luminosities. In the left panel, the accretion luminosity reaches $\sim 7.5 \times 10^{52}$ erg s^{-1} for ν_e and $\bar{\nu}_e$ and $\sim 4.1 \times 10^{52}$ erg s^{-1} for ν_x. The post-bounce times, when those accretion luminosities reach their maxima, as well as their peak values, are in good agreement with O'Connor et al. (2018). At around $t_{pb} \sim 240$ ms, the Si–O interface accretes and the mass accretion rate suddenly drops. Consequently, $L_{\nu_e,\bar{\nu}_e}$ significantly decreases. Afterward, it enters the convection-dominant phase and the neutrino profile in multi-D model starts to diverge from that in spherically symmetric model. Indeed, due to the vigorous convection motions, our neutrino luminosities show systematically higher values in all flavors than those in the 1D models of O'Connor et al. (2018), exhibiting roughly 25% and 100% increases for $L_{\nu_e,\bar{\nu}_e}$ and L_{ν_x}, respectively, at $t_{pb} = 400$ ms. Such a higher neutrino luminosity in the multi-D model reflects the effects of PNS convection around the neutrino sphere (Buras et al. 2006).

Regarding the neutrino mean energy (right panel), we again find a result consistent with two reference models in O'Connor et al. (2018), at least for the first ∼100 ms after bounce. During that early epoch, ε_{ν_e} reaches its minimum value of ∼9 MeV at $t_{pb} \sim 50$ ms. The value of $\varepsilon_{\bar{\nu}_e}$ is higher than ε_{ν_e}, preserving the

deviation $\varepsilon_{\bar{\nu}_e} - \varepsilon_{\nu_e}$ to be $\sim$3 MeV throughout most of the post-bounce phase. This feature is also seen in O'Connor et al. (2018). Meanwhile, ε_{ν_x} stays at $\sim$17 MeV just after bounce $t_{\rm pb} \lesssim 100$ ms, and then gradually increases, though the increase rate is not so high as those of ε_{ν_e} and $\varepsilon_{\bar{\nu}_e}$. Due to the multi-D effects, all the mean neutrino energies become systematically higher than those of the 1D results, especially in the late post-bounce phase $t_{\rm pb} \gtrsim 200$ ms. From these comparisons, we conclude that the new neutrino transport method in a mixed frame of the cylindrical and Cartoon coordinates works consistently with other numerical codes and is capable of performing CCSN simulations.

ORCID iDs

Takami Kuroda https://orcid.org/0000-0001-5168-6792
Tobias Fischer https://orcid.org/0000-0003-2479-344X
Tomoya Takiwaki https://orcid.org/0000-0003-0304-9283
Kei Kotake https://orcid.org/0000-0003-2456-6183

References

Abbasi, R., Abdou, Y., Abu-Zayyad, T., et al. 2011, A&A, 535, A109
Abbott, B. P., Abbott, R., Abbott, T. D., et al. 2018, LRR, 21, 3
Abe, K., Abe, T., Aihara, H., et al. 2011, arXiv:1109.3262
Alcubierre, M., Brügmann, B., Holz, D., et al. 2001, IJMPD, 10, 273
Andresen, H., Glas, R., & Janka, H. T. 2021, MNRAS, 503, 3552
Andresen, H., Müller, B., Müller, E., & Janka, H.-T. 2017, MNRAS, 468, 2032
Annala, E., Gorda, T., Kurkela, A., Nättilä, J., & Vuorinen, A. 2020, NatPh, 16, 907
Antoniadis, J., Freire, P. C. C., Wex, N., et al. 2013, Sci, 340, 448
Bastian, N.-U. F. 2021, PhRvD, 103, 023001
Bauswein, A., Bastian, N.-U. F., Blaschke, D. B., et al. 2019, PhRvL, 122, 061102
Baym, G., Hatsuda, T., Kojo, T., et al. 2018, RPPh, 81, 056902
Bazavov, A., Bhattacharya, T., DeTar, C., et al. 2014, PhRvD, 90, 094503
Bazavov, A., Ding, H. T., Hegde, P., et al. 2019, PhLB, 795, 15
Benić, S., Blaschke, D., Alvarez-Castillo, D. E., Fischer, T., & Typel, S. 2015, A&A, 577, A40
Berdermann, J., Blaschke, D., Fischer, T., & Kachanovich, A. 2016, PhRvD, 94, 123010
Bilous, A. V., Watts, A. L., Harding, A. K., et al. 2019, ApJL, 887, L23
Blondin, J. M., Mezzacappa, A., & DeMarino, C. 2003, ApJ, 584, 971
Bollig, R., Yadav, N., Kresse, D., et al. 2021, ApJ, 915, 28
Borsányi, S., Fodor, Z., Hoelbling, C., et al. 2014, PhLB, 730, 99
Bruenn, S. W. 1985, ApJS, 58, 771
Bugli, M., Guilet, J., & Obergaulinger, M. 2021, MNRAS, 507, 443
Buras, R., Janka, H.-T., Rampp, M., & Kifonidis, K. 2006, A&A, 457, 281
Burrows, A., & Vartanyan, D. 2021, Natur, 589, 29
Carter, G. W., & Prakash, M. 2002, PhLB, 525, 249
Chan, C., Müller, B., Heger, A., Pakmor, R., & Springel, V. 2018, ApJL, 852, L19
Cromartie, H. T., Fonseca, E., Ransom, S. M., et al. 2020, NatAs, 4, 72
Danielewicz, P., Lacey, R., & Lynch, W. G. 2002, Sci, 298, 1592
Demorest, P. B., Pennucci, T., Ransom, S. M., Roberts, M. S. E., & Hessels, J. W. T. 2010, Natur, 467, 1081
Drake, A. J., Djorgovski, S. G., Prieto, J. L., et al. 2010, ApJL, 718, L127
Fischer, T. 2016, A&A, 593, A103
Fischer, T. 2021, EPJA, 57, 270
Fischer, T., Bastian, N.-U. F., Wu, M.-R., et al. 2018, NatAs, 2, 980
Fischer, T., Wu, M.-R., Wehmeyer, B., et al. 2020, ApJ, 894, 9
Fonseca, E., Cromartie, H. T., Pennucci, T. T., et al. 2021, ApJL, 915, L12
Fryer, C. L., Woosley, S. E., & Hartmann, D. H. 1999, ApJ, 526, 152
Hamuy, M. 2003, ApJ, 582, 905
Hannestad, S., & Raffelt, G. 1998, ApJ, 507, 339
Heger, A., Fryer, C. L., Woosley, S. E., Langer, N., & Hartmann, D. H. 2003, ApJ, 591, 288
Hempel, M., Fischer, T., Schaffner-Bielich, J., & Liebendörfer, M. 2012, ApJ, 748, 70
Hobbs, T. J., Alberg, M., & Miller, G. A. 2016, PhRvC, 93, 052801
Horowitz, C. J. 2002, PhRvD, 65, 043001
Horowitz, C. J., Caballero, O. L., Lin, Z., O'Connor, E., & Schwenk, A. 2017, PhRvC, 95, 025801
Hyper-Kamiokande Proto-Collaboration, Abe, K., & Abe, K. 2018, PTEP, 2018, 063C01
Iwamoto, K., Mazzali, P. A., Nomoto, K., et al. 1998, Natur, 395, 672
Janka, H.-T., Melson, T., & Summa, A. 2016, ARNPS, 66, 341
Jerkstrand, A., Maeda, K., & Kawabata, K. S. 2020, Sci, 367, 415
Juodagalvis, A., Langanke, K., Hix, W. R., Martínez-Pinedo, G., & Sampaio, J. M. 2010, NuPhA, 848, 454
Kaltenborn, M. A. R., Bastian, N.-U. F., & Blaschke, D. B. 2017, PhRvD, 96, 056024
Kawahara, H., Kuroda, T., Takiwaki, T., Hayama, K., & Kotake, K. 2018, ApJ, 867, 126
Kitaura, F. S., Janka, H.-T., & Hillebrandt, W. 2006, A&A, 450, 345
Kotake, K., Takiwaki, T., Fischer, T., Nakamura, K., & Martínez-Pinedo, G. 2018, ApJ, 853, 170
Kurkela, A., Fraga, E. S., Schaffner-Bielich, J., & Vuorinen, A. 2014, ApJ, 789, 127
Kuroda, T. 2021, ApJ, 906, 128
Kuroda, T., Arcones, A., Takiwaki, T., & Kotake, K. 2020, ApJ, 896, 102
Kuroda, T., Kotake, K., & Takiwaki, T. 2016a, ApJL, 829, L14
Kuroda, T., Kotake, K., Takiwaki, T., & Thielemann, F.-K. 2018, MNRAS, 477, L80
Kuroda, T., Takiwaki, T., & Kotake, K. 2014, PhRvD, 89, 044011
Kuroda, T., Takiwaki, T., & Kotake, K. 2016b, ApJS, 222, 20
Lattimer, J. M., & Swesty, F. 1991, NuPhA, 535, 331
Liebendörfer, M., Messer, O. E. B., Mezzacappa, A., et al. 2004, ApJS, 150, 263
Liebendörfer, M., Mezzacappa, A., Thielemann, F.-K., et al. 2001, PhRvD, 63, 103004
Lund, T., Marek, A., Lunardini, C., Janka, H.-T., & Raffelt, G. 2010, PhRvD, 82, 063007
Marek, A., & Janka, H.-T. 2009, ApJ, 694, 664
Melson, T., Janka, H.-T., Bollig, R., et al. 2015a, ApJL, 808, L42
Melson, T., Janka, H.-T., & Marek, A. 2015b, ApJL, 801, L24
Mezzacappa, A., Marronetti, P., Landfield, R. E., et al. 2020, PhRvD, 102, 023027
Miller, M. C., Lamb, F. K., Dittmann, A. J., et al. 2019, ApJL, 887, L24
Miller, M. C., Lamb, F. K., Dittmann, A. J., et al. 2021, ApJL, 918, L28
Moriya, T. J., Blinnikov, S. I., Tominaga, N., et al. 2013, MNRAS, 428, 1020
Morozova, V., Radice, D., Burrows, A., & Vartanyan, D. 2018, ApJ, 861, 10
Mösta, P., Roberts, L. F., Halevi, G., et al. 2018, ApJ, 864, 171
Müller, B. 2015, MNRAS, 453, 287
Müller, B. 2020, LRCA, 6, 3
Müller, B., & Janka, H.-T. 2015, MNRAS, 448, 2141
Müller, B., & Janka, H.-T. 2014, ApJ, 788, 82
Müller, B., Janka, H.-T., & Marek, A. 2013, ApJ, 766, 43
Murphy, J. W., Ott, C. D., & Burrows, A. 2009, ApJ, 707, 1173
Nagakura, H., Burrows, A., & Vartanyan, D. 2021a, MNRAS, 506, 1462
Nagakura, H., Burrows, A., Vartanyan, D., & Radice, D. 2021b, MNRAS, 500, 696
Nagakura, H., Iwakami, W., Furusawa, S., et al. 2018, ApJ, 854, 136
Nakamura, K., Takiwaki, T., & Kotake, K. 2019, PASJ, 71, 98
Nakazato, K., Sumiyoshi, K., & Yamada, S. 2013, A&A, 558, A50
Nomoto, K., Tominaga, N., Umeda, H., Kobayashi, C., & Maeda, K. 2006, NuPhA, 777, 424
Obergaulinger, M., & Aloy, M. Á. 2021, MNRAS, 503, 4942
O'Connor, E. 2015, ApJS, 219, 24
O'Connor, E., Bollig, R., Burrows, A., et al. 2018, JPhG, 45, 104001
O'Connor, E., & Ott, C. D. 2011, ApJ, 730, 70
Pan, K.-C., Liebendörfer, M., Couch, S. M., & Thielemann, F.-K. 2018, ApJ, 857, 13
Radice, D., Abdikamalov, E., Ott, C. D., et al. 2018, JPhG, 45, 053003
Radice, D., Burrows, A., Vartanyan, D., Skinner, M. A., & Dolence, J. C. 2017, ApJ, 850, 43
Reddy, S., Prakash, M., Lattimer, J. M., & Pons, J. A. 1999, PhRvC, 59, 2888
Riley, T. E., Watts, A. L., Ray, P. S., et al. 2021, ApJL, 918, L27
Sagert, I., Fischer, T., Hempel, M., et al. 2009, PhRvL, 102, 081101
Salathe, M., Ribordy, M., & Demirörs, L. 2012, APh, 35, 485
Sedov, L. I. 1959, Similarity and Dimensional Methods in Mechanics (New York: Academic Press)
Shibagaki, S., Kuroda, T., Kotake, K., & Takiwaki, T. 2021, MNRAS, 502, 3066
Shibata, M. 2000, PThPh, 104, 325
Shibata, M., & Sekiguchi, Y.-I. 2003, PhRvD, 68, 104020
Smith, N., Li, W., Foley, R. J., et al. 2007, ApJ, 666, 1116
Sotani, H., & Sumiyoshi, K. 2019, PhRvD, 100, 083008

Sotani, H., & Sumiyoshi, K. 2021, MNRAS, 507, 2766
Sotani, H., & Takiwaki, T. 2020, MNRAS, 498, 3503
Sumiyoshi, K., Yamada, S., Suzuki, H., et al. 2005, ApJ, 629, 922
Sumiyoshi, K., Yamada, S., & Suzuki, H. 2007, ApJ, 667, 382
Takahashi, K., Umeda, H., & Yoshida, T. 2014, ApJ, 794, 40
Takeda, M., Hiranuma, Y., Kanda, N., et al. 2021, PhRvD, 104, 084063
Takiwaki, T., & Kotake, K. 2018, MNRAS, 475, L91
Takiwaki, T., Kotake, K., & Suwa, Y. 2012, ApJ, 749, 98
Takiwaki, T., Kotake, K., & Suwa, Y. 2014, ApJ, 786, 83
Takiwaki, T., Kotake, K., & Suwa, Y. 2016, MNRAS, 461, L112
Tamborra, I., Hanke, F., Müller, B., Janka, H.-T., & Raffelt, G. 2013, PhRvL, 111, 121104
Tamborra, I., Raffelt, G., Hanke, F., Janka, H.-T., & Müller, B. 2014, PhRvD, 90, 045032
Torres-Forné, A., Cerdá-Durán, P., Passamonti, A., Obergaulinger, M., & Font, J. A. 2019, MNRAS, 482, 3967
Typel, S., Röpke, G., Klähn, T., Blaschke, D., & Wolter, H. H. 2010, PhRvC, 81, 015803
Umeda, H., & Nomoto, K. 2008, ApJ, 673, 1014
Vartanyan, D., Burrows, A., & Radice, D. 2019, MNRAS, 489, 2227
Witt, M., Psaltis, A., Yasin, H., et al. 2021, ApJ, 921, 19
Wongwathanarat, A., Müller, E., & Janka, H. T. 2015, A&A, 577, A48
Woosley, S. E., Blinnikov, S., & Heger, A. 2007, Natur, 450, 390
Woosley, S. E., & Heger, A. 2007, PhR, 442, 269
Woosley, S. E., Heger, A., & Weaver, T. A. 2002, RvMP, 74, 1015
Yadav, N., Müller, B., Janka, H. T., Melson, T., & Heger, A. 2020, ApJ, 890, 94
Yanagisawa, K., Jia, D., Hirobayashi, S., et al. 2019, PTEP, 2019, 063F01
Yoshida, T., Takiwaki, T., Aguilera-Dena, D. R., et al. 2021, MNRAS, 506, L20
Yoshida, T., Takiwaki, T., Kotake, K., et al. 2019, ApJ, 881, 16
Yoshida, T., Takiwaki, T., Kotake, K., et al. 2021, ApJ, 908, 44
Zha, S., O'Connor, E. P., Chu, M.-C., Lin, L.-M., & Couch, S. M. 2020, PhRvL, 125, 051102
Zha, S., O'Connor, E. P., & da Silva Schneider, A. 2021, ApJ, 911, 74